

# Detection, photometry and slitless radial velocities of 535 planetary nebulae in the flattened elliptical galaxy NGC 4697<sup>1</sup>

R. H. Méndez and A. Riffeser

*Munich University Observatory, Scheinerstr. 1, 81679 Munich, Germany*

[mendez@usm.uni-muenchen.de](mailto:mendez@usm.uni-muenchen.de)

R.-P. Kudritzki

*Institute for Astronomy, University of Hawaii, 2680 Woodlawn Drive, Honolulu, Hawaii 96822*

M. Matthias

*Munich University Observatory, Scheinerstr. 1, 81679 Munich, Germany*

K. C. Freeman

*Mt. Stromlo and Siding Spring Observatories, Weston Creek P.O., ACT 2611, Australia*

M. Arnaboldi and M. Capaccioli

*Osservatorio Astronomico di Capodimonte, V. Moiariello 16, Napoli 80131, Italy*

and

O. Gerhard

*Astronomisches Institut, Universität Basel, CH-4102 Binningen, Switzerland*

## ABSTRACT

We have detected 535 planetary nebulae (PNs) in the flattened elliptical galaxy NGC 4697, using the classic on-band, off-band filter technique with the Focal Reducer and Spectrograph (FORS) at the Cassegrain focus of the first 8-meter telescope unit of the ESO Very Large Telescope. From our photometry we have built the [O III]  $\lambda 5007$  planetary nebula luminosity function (PNLF) of NGC 4697. It indicates a distance of  $(10.5 \pm 1)$  Mpc to this galaxy, in good agreement with the distance obtained from surface brightness fluctuations and substantially smaller than a previous estimate of 24 Mpc used in earlier dynamical

studies. The PNLF also provides an estimate of the specific PN formation rate:  $(6 \pm 2) \times 10^{-12}$  PNs per year per solar luminosity. Combining the information from on-band images with PN positions on dispersed, slitless grism images, we have obtained radial velocities for 531 of the 535 PNs. We describe the slitless velocity method, and the calibration procedures we have followed. The radial velocities have errors of about  $40 \text{ km s}^{-1}$  and provide kinematic information up to a distance of almost three effective radii from the nucleus. Some rotation is detected in the outer regions, but the rotation curve of this galaxy appears to drop beyond one effective radius. Assuming an isotropic velocity distribution, the velocity dispersion profile is consistent with no dark matter within three effective radii of the nucleus (however, some dark matter can be present if the velocity distribution is anisotropic). We obtain a blue mass-to-light ratio of 11. Earlier  $M/L$  ratios for NGC 4697 were too small, because of the too large distance used for their derivation.

*Subject headings:* galaxies: individual (NGC 4697) — galaxies: kinematics and dynamics — galaxies: distances — planetary nebulae: general — techniques: radial velocities

## 1. Introduction

Planetary nebulae (PNe) in early-type galaxies are extremely useful as distance indicators, through their luminosity function (PNLF) (e.g. Jacoby, Ciardullo, & Ford 1990; Jacoby 1997; Méndez 1999; Ferrarese et al. 2000), and also as test particles to study the dark matter distribution in the outskirts of those galaxies. A classic example of this second use is the work on 433 PNe in NGC 5128 by Hui et al. (1995). Similar attempts involving more distant galaxies observed with 4m-class telescopes have resulted in very limited samples; typically only 20 to 70 PN velocities could be measured (e.g. Ciardullo, Jacoby, & Dejonghe 1993; Tremblay, Merritt, & Williams 1995; Arnaboldi et al. 1994, 1996, 1998). PN samples larger by at least one order of magnitude are needed for reliable dynamical analyses (e.g. Merritt & Saha 1993); the best results would probably be obtained by combining a large PN sample with deep absorption-line spectroscopy, using e.g. the method followed by Saglia et al. (2000).

---

<sup>1</sup>Based on observations collected at the European Southern Observatory, Cerro Paranal, Chile; ESO programme 63.I-0008

The observational situation has recently improved. Given a sufficiently luminous early-type galaxy, at a distance of 10-15 Mpc, and working with 8m telescopes, now it is possible to detect 500 PNs and measure their radial velocities in a reasonable amount of time. The purpose of this paper is to describe these new capabilities and report on their first practical application.

FORS1, the first spectrograph to become available at the ESO VLT, has some multi-object capabilities, supporting 19 slits. However this observing mode would not be suitable for a project involving hundreds of PNs. We decided to use FORS1 in a different way (slitless radial velocities) to be explained in section 2.

As our first target we selected the flattened elliptical galaxy NGC 4697, located in the Virgo Southern Extension. Concerning dark matter content, flattened ellipticals are almost unexplored. Most of the information accumulated about dark matter in ellipticals comes from studies of hot, X-ray emitting gas (e.g. Loewenstein & White 1999) and from dynamical analyses of integrated absorption-line spectra of luminous, slowly rotating, nearly round ellipticals (e.g. Gerhard et al. 2000). There is however an interesting study of the flattened elliptical NGC 720 by Buote and Canizares (1994, 1997), based on ROSAT and ASCA X-ray observations. These authors find evidence for a flattened dark matter halo around NGC 720.

According to Garcia (1993) NGC 4697 belongs to a group of 18 galaxies, but none of the other 17 is closer than 30 arc minutes to our target. X-ray observations with ROSAT (see Sansom, Hibbard, & Schweizer 2000), suggest a rather small amount of associated hot gas. More recent observations with Chandra (Sarazin, Irwin, & Bregman 2000) show that in fact most of the detected X-ray emission is resolved into point sources, mostly low-mass X-ray binaries. NGC 4697 must have lost most of its interstellar gas. Is this a hint that this galaxy does not have a substantial amount of dark matter? A dynamical study is, in this case, the only way to learn about the dark matter existence and distribution. Among the earlier dynamical studies of NGC 4697 we mention those by Binney, Davies, & Illingworth (1990) and Dejonghe et al. (1996), both based on photometry and kinematic data from the central, high surface brightness region within one effective radius. The data were consistent with a constant mass-to-light ratio through the studied portion of the galaxy, but were not adequate to investigate the dark matter distribution. In both papers a distance of 24 Mpc was assumed for NGC 4697. Since Tonry et al. (2000) have measured a surface brightness fluctuation (SBF) distance of 12 Mpc, we decided it would be interesting to determine a PNLF distance to NGC 4697.

In section 2 we describe the method of slitless radial velocity determinations. Section 3 describes the observations and reduction procedures. Section 4 deals with the on-band

photometry. In section 5 we build the PNLF and derive the PNLF distance to NGC 4697 and the specific PN formation rate. In section 6 we describe the radial velocity results, which are analyzed in sections 7 and 8. Section 9 gives a summary of conclusions and perspectives.

## 2. Slitless radial velocities

PNs in other galaxies can be detected by blinking two images: one taken through a narrow-band interference filter selected to transmit the redshifted [O III]  $\lambda 5007$  nebular emission line (on-band image) and another one taken through a broader filter at some nearby wavelength, avoiding strong nebular emission lines (off-band image). The PNs are visible in the first image but not in the second one. The off-band image must be deeper than the on-band image for the unambiguous detection of emission-line sources.

Suppose that after the end of the on-band exposure a grism is inserted in the light path. Nothing else is changed, the telescope is kept guiding, and we take a new exposure through both the grism and the on-band filter. Please refer to Fig. 1. All stars in the field are shifted and become short segments of length defined by the grism dispersion and by the width of the on-band filter transmission curve. The PNs (and any other emission-line point sources in the field) remain as point sources, also shifted from the position they had in the undispersed on-band image. The shift is a function of the wavelength of the nebular emission line and of position on the CCD (the grism introduces anamorphic distortion). If we can measure and calibrate this shift, then it is possible to calculate the emission-line wavelength for each detected PN, giving radial velocities for all PNs in the field with maximum efficiency, irrespective of the number and distribution of PNs in the field. Since no slits are used, there are no light losses and it is not necessary to go through the complex selection and preparation procedures typical of multi-object slit (or fiber) spectroscopy. Of course the quality of the velocities will depend on the seeing. In ideal conditions, all the images needed to find the PNs and get the kinematic information can be collected in just one observing run.

The basic idea for slitless radial velocities is quite old. A selected list of historical references can be found in Douglas & Taylor (1999). In recent times, slitless techniques for emission-line objects have been explored as alternatives to the classic multi-object technique. For example, work based on a Fabry-Perot interferometer (Tremblay, Merritt, & Williams 1995) and on counter-dispersed imaging (Douglas & Taylor 1999; Douglas et al. 2000). Here we present the simplest procedure for slitless PN radial velocities, applied for the first time with the light-collecting power of an 8-meter telescope.

Let us describe the procedure for wavelength calibration. We need to determine the

shift produced by the insertion of the grism as a function of wavelength and position on the CCD. Since we have 19 slits in FORS, we can use them for the calibration. We align the 19 slits vertically near the left edge of the CCD, and take an exposure illuminating the slits with the comparison lamp. This is the undispersed image. Then we insert the grism and take another exposure, the dispersed image. Now we move all the slits to the right, defining a new calibrating position, and repeat the sequence of two exposures. This can be repeated until we have covered the useful region of the CCD (since the grism produces a shift to the right, no calibration is possible for objects located near the right edge of the CCD). Fig. 2 shows the grid of calibration positions ( $19 \times 10$  slits) on the CCD, and Fig. 3 shows an example of undispersed and dispersed calibration images.

For all wavelength measurements, we assume that the direction of dispersion is exactly horizontal (which is not true, because there is a small amount of pincushion distortion; we will correct for this effect later) and measure the undispersed and dispersed  $x$  positions of the slits at fixed  $y$  values. With this information we can find the relation between shift and wavelength for each of the 190 calibration positions. The wavelength can be expressed as a polynomial of second order in the shift.

The procedure for PN wavelength calculation is the following: having measured the positions of a PN in the undispersed and dispersed images, select the four grid positions closest to the undispersed PN coordinates. Calculate the wavelength for each of the four grid positions, using as input the shift between dispersed and undispersed PN  $x$  coordinates (acting as if the PN was located exactly at each of the four grid positions). From these four wavelengths, obtain the final wavelength by bilinear interpolation, using the correct undispersed PN  $x, y$  coordinates.

Our decision to assume a horizontal direction of dispersion is based on the lack of any simple procedure that could help to determine the direction of dispersion for any point in the CCD. The price to pay for this simplification in the measurements is that we need a complementary set of exposures to test for the presence of systematic errors in the radial velocities, arising from the pincushion distortion mentioned above. We tested the accuracy of slitless radial velocities near the center of the field by taking undispersed and dispersed images of He 2-118, a PN of small angular size with a sufficiently well-known radial velocity,  $-164 \pm 9 \text{ km s}^{-1}$  (Schneider et al. 1983). Since it would be impractical to take many such exposures with the PN in many different places across the CCD, we decided to make multi-object through-slit (undispersed) images of NGC 7293, insert the grism, and take the corresponding multi-object spectrograms. Six such sequences, with the 19 slits aligned at different  $x$  positions across the CCD, were enough for our purposes. We aligned the 19 FORS slits along a line shown in Fig. 4. The radial velocity of NGC 7293 on this line is  $-20 \pm 10$

km s<sup>-1</sup> (Taylor 1977). The 19×6 slit positions on the CCD are shown in Fig. 5. We found empirically that the radial velocities must be corrected by a small term which is a function of the distance from the measurement point to a reference diagonal line, also shown in Fig. 5. Please refer to section 6, where we describe all the slitless radial velocity results.

The accuracy of slitless radial velocities depends on being able to ensure that the distance between undispersed and dispersed images on the CCD is not modified by mechanical deformations in the spectrograph, or guiding problems. This is not relevant during the very short exposures needed for the calibrations, but it is a matter of concern when dealing with exposures longer than 30 minutes. We will discuss this potential source of error in section 6, showing that it is of minor importance in our case.

### 3. VLT Observations and reductions

The galaxy NGC 4697 has an effective radius of 95 arc seconds (Binney, Davies, & Illingworth 1990). We decided to orient the x-axis of the CCD in the direction of the major axis, and to expose two partly overlapping fields, NE and SW of the galaxy center, with the central region appearing in both fields, to provide some degree of redundancy. We call the two fields E and W, for simplicity. They are shown in Figs. 6 and 7.

The observations were made by R.H.M. with the first Focal Reducer and low dispersion Spectrograph (FORS1) at the Cassegrain focus of Unit Telescope 1, Antu, of the ESO Very Large Telescope, Cerro Paranal, Chile, on the nights of 1999 April 19/20 and 21/22, and 2000 May 29/30, 30/31 and May 31 / June 1. FORS1 with the standard collimator gives a field of 6.8×6.8 arc minutes on a 2080×2048 CCD (pixel size 24×24  $\mu\text{m}$ ). The image scale is 0.2 arcsec/pixel.

Direct imaging was done through interference filters. The on-band and off-band filters used for NGC 4697 have the following characteristics: effective central wavelengths, in observing conditions, 5028 and 5300 Å; peak transmissions 0.76 and 0.80; equivalent widths 48.5 and 215 Å; FWHMs 60 and 250 Å. The dispersed images were obtained with grism 600B. This grism gives a dispersion of 50 Å/mm, or 1.2 Å/pixel, at 5000 Å.

Table 1 lists the most important CCD images obtained for this project. They can be divided into the following groups:

- (1) off-band, on-band, (grism + on-band) images of NGC 4697, E field
- (2) off-band, on-band, (grism + on-band) images of NGC 4697, W field

(3) on-band, (grism + on-band) multi-slit images and comparison lamp spectra through 10 different vertical arrangements of the 19 FORS slitlets, for the wavelength calibration.

(4) on-band, (grism + on-band) images of the Galactic PN He 2-118 (PN G 327.5+13.3) to test the quality of the slitless radial velocities. In this case we used another on-band filter, with effective central wavelength 4990 Å and FWHM=60 Å.

(5) on-band, (grism + on-band) multi-slit images and spectra of the Galactic PN NGC 7293 (PN G 036.1-57.1), in 6 different positions across the CCD, for complementary calibration purposes. For this PN we also used the  $\lambda$ 4990 narrow-band filter.

(6) on-band ( $\lambda$ 5028) images of the spectrophotometric standard G138-31 (Oke 1990) for the photometric calibration.

The 1999 April nights were partly clear but certainly not photometric. The seeing was around 0.7 arc seconds. We were fortunate to get two photometric nights for our flux calibrations: the two first nights in May 2000. The typical seeing was 0.8 arc sec. The third and last night was affected by sporadic cirrus clouds and poorer seeing (around 1 arc sec).

The basic CCD reductions (bias subtraction, flat-field correction using twilight flats) were made using IRAF<sup>2</sup> standard tasks.

Next, it was necessary to combine all undispersed on-band images, for E and W fields separately, to eliminate cosmic ray events and enable detection of faint PNs. Combined images were also made from the off-band images E and W and from the dispersed images E and W.

The image combinations required careful preparatory work. It is important to ensure that the distance in pixels between undispersed and dispersed PN images is not affected by incorrect registration of the images to be combined. For example, an error of 0.3 pixel in the distance between undispersed and dispersed images produces an error of 20 km s<sup>-1</sup> in radial velocity, if the dispersion is 50 Å/mm. The following procedure was followed: first of all, for each field, E and W, one pair of (undispersed, dispersed) on-band individual images, of the best possible quality, taken consecutively at the telescope, was adopted as reference images. In this way any possible displacements produced by guiding problems or deformations in the spectrograph are reduced to a minimum. We had in total four reference images (see Table 1): one pair for the E field (30T00:51 and 30T01:17) and one pair for the W field (30T23:33

---

<sup>2</sup>IRAF is distributed by the National Optical Astronomical Observatories, operated by the Association of Universities for Research in Astronomy, Inc., under contract to the National Science Foundation of the United States

and 31T00:00). All the other images, including the off-band ones, were registered upon the corresponding reference image.

For registration we used a program developed in Munich by C. A. Gössl and A. Riffeser (2001, in preparation) as part of their “image reduction pipeline”. The registration program, given a sample of well-distributed reference stars in both the reference image and the image to be registered, allows rotations, linear shifts, and (very small) scale changes, in order to obtain a coordinate transformation that minimizes the residuals of all reference stars, while preserving the point-spread-function (PSF) as much as possible. The coordinates of the reference objects in all images are obtained by a seven-parameter rotated Gaussian fit. For a star-like PSF the fit is performed within a box of  $21 \times 21$  pixels.

It turned out that the images taken in 1999 had to be slightly rotated for registration: this rotation angle was 0.2 degrees.

The quality of the registrations showed interesting differences. The registration of the undispersed E-field images was very good; using 30 reference stars the residuals were never larger than 0.1 pixel. The registration of the undispersed W-field images was not so good, particularly for the 1999 images requiring rotation. Using 44 reference stars, most of the residuals were smaller than 0.2 pixel, but some residuals for the 1999 images were as large as 0.3 pixel.

The registration of dispersed images is more difficult. We had to model the PSF within a larger box,  $121 \times 27$  pixels, with a Gaussian which is wider in the direction of dispersion. The solutions for the E-field were based on 11 bright reference stars and produced residuals below 0.2 pixel. The solutions for the W-field were based on 8 reference stars and although typical residuals were below 0.2 pixel, in the case of the 1999 grism images some residuals were as large as 0.4 pixel.

We produced the combined images, from the reference and registered images, using the IRAF task “imcombine” with “ccdclip” rejection algorithm. We made a test with the E and W combined dispersed images: we compared the positions of bright PNs visible in each reference dispersed image versus the PN positions in the corresponding combined dispersed image. The comparison was satisfactory for the E-field, but we found that a correction was needed for the W-field. The reason for this correction will be explained in next paragraph. The correction (equivalent to about 50 km/s) was mapped using 30 bright PNs well distributed in the W field, and later on applied to the PN positions measured in the combined W dispersed image. In this way we convinced ourselves that PN positions in the E and W combined dispersed images were not affected by systematic errors larger than 0.3 pixel. Therefore this source of position errors contributes at most  $20 \text{ km s}^{-1}$  to the total

uncertainty in radial velocity. We will discuss the errors more extensively in section 6.

Why was a correction needed for the positions of PNs measured in the combined dispersed W-field image? The transmission curves of narrow-band filters shift in wavelength as a function of ambient temperature, by about 0.2 Angstroms per degree Celsius. The positions of dispersed PN images are not affected, but the spectral segments of continuum sources are shifted if the temperature changes. From the information in the headers of dispersed images we know that the dispersed images in the E-field were taken with temperatures between 11.4 and 12.8 degrees Celsius. This range of temperatures is not enough to produce significant displacements. On the other hand most of the dispersed images in the W-field were taken in 1999 with temperatures around 15.5 degrees Celsius, but the reference dispersed image was taken in 2000 with a temperature of 12.4 degrees Celsius. Since we used continuum sources for registration of the dispersed images, there was a systematic difference in the PN positions, which we could detect and correct as explained above.

We extract two conclusions from this experience: first, for the highest accuracy in FORS slitless radial velocities it is better, if possible, to avoid combining images taken in different observing runs, because very probably slight rotations will be needed for the registrations, leading to less satisfactory registrations; second, all grism exposures should be long enough to provide a sufficient number of bright PNs in the field for adequate control of the quality of registration across the CCD. In future work we will try to register dispersed images using directly the brightest PN images, avoiding in this way any dependence on ambient temperature variations.

For easier PN detection and photometry in the central parts of NGC 4697, where the background is strongly varying across the field, we decided to produce images giving the differences between undispersed on-band and off-band combined frames. In ideal conditions this image subtraction should produce a flat noise frame with the emission-line sources as the only visible features. A critical requirement to achieve the desired result is perfect matching of the point spread functions (PSFs) of the two frames to be subtracted. For this purpose we applied a method for “optimal image subtraction” developed by Alard & Lupton (1998), as implemented in Munich by Gössl and Riffeser (2001, in preparation) as part of their “image reduction pipeline”. Very briefly the idea is to split the images in many subimages (in our case a few hundreds), allowing for different convolution kernels in different subimages to match one image against the other. Figures 8 and 9 show sections of the resulting difference images in the E and W fields.

We cannot use this procedure for the dispersed combined images because we do not have any off-band counterpart. Therefore in order to flatten the background and reduce the contamination of the fields by the stellar spectra, we had to use simpler methods. The

IRAF task “fmedian” was applied to the combined E and W dispersed images, with a box of  $17 \times 17$  pixels, and the resulting medianed images were subtracted from the unmedianed ones. Figures 10 and 11 show the result. Although by no means perfect, the subtraction was sufficient for our PN detections.

#### 4. PN detection and photometry

The exposure times were adjusted to obtain similar counts in undispersed and dispersed combined images. This was achieved to within about 20%. Since our main scientific drive is to produce kinematic information from the PNs, we require a detection in both the undispersed and dispersed combined images to consider a PN as confirmed. In addition we also require the object to be a point source and to be undetectable in the off-band image, to minimize confusion with emission-line sources in background galaxies. In fact several non-PN emission-line sources (brighter in the on-band but visible in the off-band, and/or extended) were detected; a list will be provided in a future paper, now in preparation.

We experimented with a variety of software for object detection, but finally decided to use the traditional blinking method, reasoning that anyway a lot of time would be needed to confirm by eye the reality of any automatic detections, particularly in the very difficult dispersed images, because of the contamination by numerous stellar spectra, even after subtracting the medianed image.

Each combined image to be blinked was subdivided into 100 subimages of  $220 \times 220$  pixels, allowing some overlap between adjacent subimages. The candidate PNs were found by blinking the on-band vs. off-band subimages, and confirmed by blinking on-band vs. dispersed. In the central regions of the galaxy the differences (on-band – off-band) were blinked vs. dispersed images, and in this case the confirmation was provided by the overlap between the E and W fields. Near the center it is difficult, in principle, to avoid contamination by emission-line sources in background galaxies. However the area affected is small and the degree of contamination is insignificant in view of the high surface density of PNs in that region. Besides, the surface brightness of the galaxy is high near the center, and any existing background sources are unlikely to be detected unless they are very bright. The radial velocities provide an additional way of identifying sources not related to NGC 4697, as we will report in section 6.

The  $x$ ,  $y$  pixel coordinates of all the candidate PNs in the undispersed and dispersed images were measured using the IRAF task “phot” with centering algorithm “centroid”. In Section 6 we will describe the procedure for radial velocity determinations; here we concen-

trate on the on-band photometry.

We will express our  $\lambda 5007$  fluxes in magnitudes  $m(5007)$ , using the definition introduced by Jacoby (1989):

$$m(5007) = -2.5 \log I(5007) - 13.74 \quad (1)$$

For the flux calibration we adopted the standard star G138-31 (Oke 1990). This star has a monochromatic flux at 5028 Å of  $1.44 \times 10^{-15}$  erg cm $^{-2}$  s $^{-1}$  Å $^{-1}$ . The flux measured through the on-band filter in erg cm $^{-2}$  s $^{-1}$  can be calculated knowing the equivalent width of the on-band filter; using equation (1) we find  $m(5007) = 19.15$  for G138-31.

Since only part of the nights were photometric, and most PNs were only measurable on the differences of combined images (on – off), we had to proceed in several steps. First of all we used IRAF task “phot” to make aperture photometry of G138-31. The FWHM of the G138-31 images was between 3 and 4.5 pixels. We adopted an aperture radius of 16 pixels; the sky annulus had an inner radius of 21 pixels and a width of 5 pixels. Exactly the same parameters were used to make aperture photometry of a set of three moderately bright stars, visible in both fields E and W, on individual CCD frames 30T00:51, 30T23:33, 31T00:42, and 31T02:12 (see Table 1), taken on the May photometric nights 29/30 and 30/31. The three “internal frame standards” are between 2 and 3 mags fainter than G138-31, and they are located far from the center of NGC 4697, to avoid background problems. None of them showed evidences of variability.

Having tied our spectrophotometric standard to the “internal frame standards”, we could switch to strictly differential photometry. We made aperture photometry of our three internal standards on the E and W on-band combined images, to determine a correction due to non-photometric conditions affecting some of the combined frames. On the same on-band combined images we subsequently made PSF-fitting daophot photometry (Stetson 1987; IRAF tasks “phot”, “psf”, “allstar”) of the three internal standards and of four bright PN candidates close to them (i.e. visible in both the E and W fields and far from the center of NGC 4697). From the aperture photometry and psf-fitting photometry of the three internal standards we determined the aperture correction. Finally, we made psf-fitting photometry of all PN candidates on the difference images (on-band – off-band), where of course no normal stars remain; we used the four selected bright PNs to tie this photometry to that of the standards. From the good internal agreement through all these steps we estimate internal errors in the photometry below 2%.

A final correction is needed to obtain physical fluxes, which requires the on-band filter peak transmission (e.g. Jacoby, Quigley, & Africano 1987). We measured the filter transmis-

sion on multi-slit CCD frames illuminated with internal flat lamps and exposed (a) through the grism and (b) through the grism + on-band filter. From our measurements we estimate that any uncertainties in the filter transmission correction cannot affect the final fluxes by more than 5%, even taking into account that the filter transmission is to some minor extent a function of position on the CCD.

After measuring the observed wavelengths of the detected emission lines (please refer to section 6) we verified that all PNs have redshifted wavelengths between 5022 and 5034 Å. None of them is shifted away from the flat peak of the on-band filter transmission curve, irrespective of PN position on the CCD, and therefore we have not made any correction to the photometry as a function of redshift.

As a further test we have used the redundancy provided by the overlap between the E and W fields: plotting magnitude differences between the two measurements (E and W) of PN candidates as a function of difference in distance from the center of the CCD, we have found a scatter diagram without any evidence of correlation.

Figure 12 shows the E on-band magnitudes  $m(5007)$  as a function of the W on-band magnitudes for 211 objects measured in both fields. From the dispersion in Fig. 12 we estimate RMS errors of 0.1 and 0.2 mag for  $m(5007)$  brighter and fainter than 26.5, respectively. For each of these 211 PNs we have adopted the average of the two  $m(5007)$  measurements.

## 5. The PNLF, distance, and PN formation rate

Knowing the apparent magnitudes  $m(5007)$  we can build the PN luminosity function. Since we are dealing with a non-uniform background, we need to produce a statistically complete sample, because the detectability of a PN varies with the background surface brightness. We operate in the following way: first we find the value of  $m(5007)$  at which the raw, uncorrected PNLF starts to show a decreasing number of PNs per bin, as we move towards fainter magnitudes. This indicates the onset of severe incompleteness (see e.g. Fig. 7 in Jacoby et al. 1989, or Fig. 2 in Jacoby et al. 1990). In our case, this “incompleteness limit” is at  $m(5007) = 27.6$ . All PNs fainter than 27.6 are subsequently ignored for PNLF purposes. If the resulting sample is statistically complete, then the surface density of PNs brighter than 27.6 anywhere in the galaxy must be proportional, in a first approximation, to the surface brightness of the galaxy at that location. We attribute any departure from this proportionality (i.e. lack of PNs) to incompleteness. In doing so we disregard a small color effect: the surface density of PNs normally decreases with increasing  $B - V$  (see e.g. the discussion in section 8 of Hui et al. 1993). Since NGC 4697 shows a small color gradient (e.g.

Table IV in Peletier et al. 1990), the PN surface density should decrease slightly towards the center. By ignoring this color effect we are in fact slightly overestimating the incompleteness.

We test for completeness by counting the number of PNs brighter than 27.6 detected in squares of a suitable size (we adopted  $220 \times 220$  pixels) and plotting this number as a function of the background counts per pixel for each square. We show this plot in Fig. 13. As expected, initially the number of detected PNs grows proportional to the background counts, until the relation ceases to be linear somewhere above 1000 counts per pixel. Therefore to ensure completeness we build the PNLF using only those PNs brighter than 27.6 that are sufficiently distant from the galaxy center to have background counts below 1000 per pixel. The zone of exclusion is an ellipse at the center of NGC 4697, with (minor, major) semiaxes of (200, 300) pixels (the image scale is 0.2 arcsec/pixel). We are left with 328 PNs, which is more than enough for a good PNLF distance determination.

The statistically complete PNLF is plotted in Fig. 14, which shows the absolute magnitudes  $M(5007)$  derived using an extinction correction of 0.105 mag (the  $E(B - V) = 0.03$  is taken from Tonry et al. 2000, who used a recent study of Galactic extinction by Schlegel, Finkbeiner, & Davis 1998), and a distance modulus  $m - M = 30.1$ . The observed PNLF is fitted with a simulated PNLF like the one used by Méndez & Soffner (1997) to fit the observed PNLF of M 31. The simulated PNLFs plotted in Fig. 14 are binned, like the observed one, into 0.2 mag intervals, and have the following characteristics: maximum final mass 0.63 solar masses,  $\mu_{max} = 1$ , and sample sizes between 2500 and 4900 PNs (see Méndez & Soffner 1997; the “sample size” is the *total* number of PNs, detected or not, that exist in the surveyed area). The fit in Fig. 14 permits an unambiguous determination of distance and sample size because the observed PNLF shows an evident change of slope.

Attempts to fit the observed PNLF at a distance modulus of 29.9 or 30.3 fail clearly. We conclude that our derived distance modulus of 30.1 has an internal error of 0.1 mag.

Now we estimate the total error budget. Following the careful discussion in Jacoby et al. (1990), we distinguish between “possible systematic” and random errors. The net systematic error is exactly the same as in Jacoby et al. (1990), i.e. 0.13 mag, including the possible error in the distance to M 31, in the modeling of the PNLF and in the foreground extinction. The random contributions in our case are: 0.1 mag from the fit to the PNLF, as mentioned above; 0.05 mag from the photometric zero point; and 0.05 mag from the filter calibration. If we combine all these errors quadratically we conclude that the total error bar for the distance modulus must be  $\pm 0.18$  mag.

We find good agreement, within the uncertainties, with the SBF distance modulus  $30.35 \pm 0.2$  reported by Tonry et al. (2000). Our distance modulus is equivalent to a distance of

10.5 Mpc. Note that the small difference between the PNLF and SBF distances is in the same sense as for other galaxies more distant than 10 Mpc; above that limit SBF distances are systematically larger than PNLF distances (see Méndez 1999).

It is also possible to get a PNLF distance using the analytical representation (exponential + cutoff) proposed by Ciardullo et al. (1989). This is shown in Fig. 15. The shape of the analytical PNLF is somewhat different, but the resulting distance modulus is the same.

After estimating the sample size in Fig. 14 we can calculate the specific PN formation rate  $\dot{\xi}$ , in PNs per year per solar luminosity, using the following expression:

$$n_{\text{PN}} = \dot{\xi} L_T t_{\text{PN}} \quad (2)$$

where  $n_{\text{PN}}$  is the sample size,  $L_T$  is the total bolometric luminosity of the sampled population, expressed in solar luminosities, and  $t_{\text{PN}}$  is the lifetime of a PN, for which we have adopted 30 000 years in the PNLF simulations.

We need to estimate the sampled luminosity in NGC 4697. From  $B_T=10.14$ ,  $B-V=0.89$  (de Vaucouleurs et al. 1991),  $A_B=0.13$  (Tonry et al. 2000) and a bolometric correction of  $-0.78$  mag, we obtain an extinction-corrected apparent bolometric magnitude 8.34. Using the distance modulus 30.1 and a solar  $M_{\text{bol}} = 4.72$ , the total bolometric luminosity of NGC 4697 is  $3.9 \times 10^{10}$  solar luminosities. Since we omitted the central ellipse to obtain our statistically complete PN sample, and estimating from our images that the central ellipse contributes 50% of the total luminosity, we conclude that the sampled luminosity is  $L_T = 1.95 \times 10^{10}$  solar luminosities. Adopting  $n_{\text{PN}} = 3500$ , we get  $\dot{\xi} = (6 \pm 2) \times 10^{-12}$ .

Transforming our value of  $\dot{\xi}$  into a specific PN density  $\alpha_{2.5}$  in PNs per solar luminosity, as used e.g. by Jacoby et al. (1990) and Ciardullo (1995), we find  $\alpha_{2.5} = 15 \times 10^{-9}$ . Thus NGC 4697 fits quite well into the empirical relation between  $\alpha_{2.5}$  and absolute  $B$  magnitude (see Fig. 2 of Ciardullo 1995).

## 6. Radial velocities: results and discussion

In section 2 we have explained the procedure to measure slitless radial velocities, and here we present the results. In what follows we will refer to heliocentric radial velocities determined with the slitless method simply as “velocities”. We consider first the velocities of NGC 7293 measured at the 114 positions shown in Fig.5. All velocities were correct to within  $50 \text{ km s}^{-1}$ , but closer inspection showed a trend as a function of position on the CCD. This trend cannot be attributed to the velocity field in NGC 7293, and must be due to the

pincushion distortion produced by the FORS optics. We discovered empirically that this behavior could be modeled as a cubic parabola if we plotted the velocities as a function of the distance from the undispersed position to the diagonal reference line shown in Fig. 5. These distances are defined to be positive above the reference line, and negative below; see Fig. 16. We introduced an empirical correction designed to give the expected velocity ( $-20 \text{ km s}^{-1}$ ) irrespective of position on the CCD. The result of applying the correction is shown in Fig. 17. Our calibrations give velocities with errors below  $20 \text{ km s}^{-1}$ . We verified this using the test exposures of the PN He 2-118: the velocities obtained from observations in two different nights are  $-175$  and  $-184 \text{ km s}^{-1}$ , in good agreement with the catalog velocity ( $-164 \text{ km s}^{-1}$ ).

Now concerning NGC 4697: if we add quadratically the calibration errors and the errors from image registration (Section 3) we get errors of about  $30 \text{ km s}^{-1}$ . However there is another source of errors: spectrograph deformations and guiding problems during long exposures. The only way of testing the impact of this kind of errors is to compare velocities obtained from different pairs of (undispersed, dispersed) long exposures. For this purpose the redundancy between the E and W fields becomes very useful. In Fig. 18 we compare the velocities of 165 PNs measured in both fields. The standard deviation in Fig. 18 is  $36 \text{ km s}^{-1}$ . We conclude that spectrograph deformations and guiding errors contribute only marginally, if at all, to the total uncertainty in the velocities, which we estimate to be  $40 \text{ km s}^{-1}$ . We have adopted the average of both velocity measurements for the 165 PNs in Fig. 18.

Most of the velocities of PNs in NGC 4697 are distributed between  $900$  and  $1600 \text{ km s}^{-1}$ . We found three emission-line point sources that gave very discrepant velocities if interpreted as  $\lambda 5007$  emitters:  $2100$ ,  $2050$ , and  $1800 \text{ km s}^{-1}$ . We rejected these three objects as PNs, assuming that they are high-redshift, background emission-line galaxies. Of course our PNLF plots do not include them either. These three sources will be described in a future paper, now in preparation, which will bring a full catalogue of the 535 PNs in NGC 4697 and a list of non-PN sources. It is conceivable that there are a few additional contaminants which we could not identify as non-PNs; but their possible existence will not affect the conclusions we present in what follows.

Fig. 19 shows the  $x$ ,  $y$  coordinates of the 535 PNs relative to the center of light of NGC 4697. The position of this center can be measured with errors below 1 pixel. The PN distribution has the shape of a rectangle: there must be more PNs beyond the limits of our survey. However, to detect and study them will be quite time consuming, because for low PN surface densities there will be more contamination with background sources, and the only way to confirm any on-band point source as a PN will be to take a deep spectrum and

detect the pair of [O III] emission lines  $\lambda\lambda 4959, 5007$ .

Fig. 20 shows the velocities of 531 PNs as a function of the  $x$  coordinate relative to the center in pixels. Four PNs were too far to the right of the W field to permit a velocity measurement. Figure 21 shows the same 531 velocities as a function of the  $y$  coordinate. The average velocity of the 531 PNs is  $1270 \text{ km s}^{-1}$ , in good agreement with the most accurate velocities quoted in the literature for NGC 4697, namely 1236, 1250 and  $1307 \text{ km s}^{-1}$  in de Vaucouleurs et al. (1991), da Costa et al. (1998), and Trager et al. (2000), respectively. Our velocity for NGC 4697 has an uncertainty of about  $15 \text{ km s}^{-1}$ , if we take into account a velocity dispersion of the order of  $150 \text{ km s}^{-1}$  (see section 8 below); the number of PNs we measured; and the possible systematic error of  $\pm 10 \text{ km s}^{-1}$  in our velocities from the calibration procedure using NGC 7293.

## 7. Rotation

Since we have the CCD x-axis oriented in the direction of the major axis of NGC 4697, we first investigate the rotation simply by defining 8 subsamples along the x-axis and calculating the average velocity for each subsample (the subsamples are not equally spaced in  $x$  because we want to ensure a minimum number of PNs per subsample). The result is shown in Fig. 22, compared with rotation data derived from long-slit spectroscopy along the major axis in the inner region of the galaxy by Binney et al. (1990). Their effective radius  $R_e = 95$  arc seconds is equivalent to 475 pixels in our CCD. They did not find any rotation along the minor axis (that is to say around the major axis). We have subdivided the PN data into four subsamples along the minor axis, confirming that there is no evidence of rotation in that direction; the average velocities from the 4 subsamples are, in order of increasing  $y$  values, 1244, 1280, 1278, and  $1260 \text{ km s}^{-1}$ .

On the other hand, as expected, the PNs in Fig. 22 indicate some rotation along the major axis. The PNs appear to follow the sense of rotation indicated by the absorption-line studies: there are noticeable deviations in the average PN velocities at  $0.5 R_e$ , where absorption lines indicate maximum rotation velocity. The signature of rotation from the PNs is diluted by the extension of our 8 subsamples in the  $y$  direction: Binney et al. (1990) measured slower rotation along lines parallel to, but 10 and 20 arc sec away from the major axis. In order to illustrate this dilution effect, Fig. 23 shows the result of defining PN subsamples restricted to a smaller range of  $y$  values. The new PN subsamples cover a slot 20 arc sec wide along the major axis. A narrower slot would give too small PN subsamples. Now the average PN velocities follow the absorption line data much more closely, except near the center, where some dilution of rotation is still evident. But Fig. 23 indicates that

the PNs behave kinematically like the stellar population.

Consider now the outer regions: the extreme points in Figs. 22 and 23 give a difference in velocity of about  $90 \text{ km s}^{-1}$ , a rather small quantity if we compare with the  $220 \text{ km s}^{-1}$  derived inside from the absorption-line data. The rotation curve of this galaxy appears to drop beyond one effective radius.

## 8. Line-of-sight velocity dispersion and $M/L$ ratio

In order to study the run of the line-of-sight velocity dispersion as a function of the angular distance from the center, we defined a central zone of radius 70 arc seconds and 2 intermediate rings, with boundaries at 140 and 200 arc seconds. Each of these zones was subdivided into SW (receding) and NE (approaching), to minimize the effect of rotation on the dispersions (since we know from previous work that in this galaxy dispersion is more important than rotation, we do not expect any remaining residual rotation to affect our conclusions concerning dispersion). To the 6 central zones we added two outer zones, again SW and NE, with PNs having  $x$  coordinates larger than 200 arc seconds relative to the center. The numbers of PNs within each zone are listed in the caption to Fig. 24, where we show the resulting line-of-sight velocity dispersions, which have been corrected to compensate for the effect of measurement errors of  $40 \text{ km s}^{-1}$ . We also show the velocity dispersions derived from absorption-line spectra along the major axis by Binney et al. (1990). In the central region the integrated light data and PN data are in excellent agreement; the dispersion from PNs is slightly (but not significantly) larger.

We derive an estimate of the total mass and mass distribution of NGC 4697 using an analytical model proposed by Hernquist (1990). This model is spherical, nonrotating and isotropic, and we use it just as a first approximation to the dynamical problem. The run of the line-of-sight velocity dispersion predicted from this model is shown in Fig. 24. The fit was obtained adopting a total mass of  $1.9 \times 10^{11}$  solar masses and  $R_e=95$  arc seconds, which is equivalent to 4823 pc for the distance modulus  $m - M=30.1$ . We tried to fit both the absorption-line data and the PN data; a fit using only the PN data would have required a total mass of  $2.0 \times 10^{11}$  solar masses.

Now we can estimate the  $M/L$  ratio in blue light: knowing the extinction-corrected  $B_T=10.0$ , the distance modulus 30.1 and the solar  $B$  absolute magnitude 5.48, we obtain for NGC 4697 a blue luminosity of  $1.7 \times 10^{10}$  solar luminosities, which gives  $(M/L)_B=11$ . In earlier studies (e.g. Dejonghe et al. 1996), based on more adequate 2-integral and 3-integral models, the adoption of a too large distance (24 Mpc) led to a too small  $(M/L)_B \sim 5$ . We

have verified that the Hernquist model gives, for a distance of 24 Mpc, the same  $M/L$  ratio obtained by Dejonghe et al. We have also followed a simple dynamical analysis similar to that used by Hui et al. (1995) in their study of NGC 5128, finding again a total mass of about  $2 \times 10^{11}$  solar masses for NGC 4697.

A blue  $M/L$  ratio near 10 is consistent with the predictions from stellar population models like those of Maraston (1998, and private communication) for ages of the order of 10 Gyr if we adopt a Salpeter IMF and a metallicity slightly higher than solar (according to recent studies by Trager et al. (2000) and Thomas & Maraston (in preparation) the [Z/H] ratio of NGC 4697 is near 0.1).

Since the Hernquist model assumes a constant  $M/L$  ratio, the good fit in Fig. 24 indicates that we have found no evidence of dark matter within  $3 R_e$  of the galaxy’s nucleus. This result is consistent with the apparent drop of rotation velocity in the outer parts, mentioned in the previous section, and with the absence of hot gas, mentioned in the introduction.

Note however that the Hernquist model assumes an isotropic velocity distribution. If there is anisotropy (e.g. a preponderance of radial orbits outside) then some dark matter can be present. To make a more careful study of the dynamics of NGC 4697 is beyond the scope of this paper. In the near future we expect to make VLT+FORS long-slit spectroscopy of NGC 4697 at different positions and position angles, extending the absorption-line studies to  $2 R_e$  if possible. Combining this additional information with the PN data we can then make a more detailed study based on 3-integral models adapted to a flattened system. That will be the subject of a future paper.

## 9. Recapitulation and perspectives

We have detected 535 PNs in NGC 4697 and measured their brightnesses and radial velocities. We have built the [O III]  $\lambda 5007$  PNLF and used it to estimate the distance to NGC 4697,  $(10.5 \pm 1)$  Mpc, in good agreement with the surface brightness fluctuation distance, and its specific PN formation rate,  $(6 \pm 2) \times 10^{-12}$  PNs per year per solar luminosity.

We have completed the first large-scale experience with a method of slitless radial velocity determination for emission-line sources, based on direct on-band plus dispersed grism+on-band exposures. The method is efficient and easy to calibrate, producing velocities for all detected emission-line sources in the field, irrespective of their number and distribution, with errors of the order of  $40 \text{ km s}^{-1}$  in the specific case of VLT+FORS. The errors may become smaller if all observations are made within a single observing run, because one of the main sources of uncertainty is the error in registration when slight rotations of the dispersed

frames are needed.

We have provided PN kinematic information covering the full galaxy up to a distance of almost three effective radii from the nucleus. Some rotation is detected in the outer regions, but the rotation curve of this galaxy appears to drop beyond one effective radius. Assuming an isotropic velocity distribution, the velocity dispersion profile is consistent with no dark matter within three effective radii of the nucleus (however, some dark matter can be present if the velocity distribution is anisotropic). A more detailed dynamical study of NGC 4697 is postponed until we secure additional integrated light data. We obtain a blue mass-to-light ratio of 11. Earlier  $M/L$  ratios for NGC 4697 were too small, because of the too large distance used for their derivation.

The work we have presented opens several interesting possibilities for future projects. Dynamical studies based on PNs can now be extended to many field and cluster elliptical galaxies in the distance range from 10 to at least 20 Mpc, without all the trouble associated with planning and executing multi-object spectroscopy for hundreds of sources. Our empirical knowledge of dark matter distributions in ellipticals will certainly increase. In addition, given enough telescope time, it will be possible to make abundance determinations for many of the brightest detected PNs; for example, we would need 10 to 15 hours of total exposure time with FORS to measure abundances in the 10 brightest PNs of NGC 4697. It would seem that we are getting close to being able to explore a PN abundance approach to metallicity gradients as well as to the still unsolved problem of age-metallicity degeneracy in elliptical galaxies.

## 10. Acknowledgments

We thank the anonymous referee for careful reading and useful comments.

## REFERENCES

Alard, C., & Lupton, R. H. 1998, *ApJ*, 503, 325

Arnaboldi, M., Freeman, K. C., Gerhard, O., et al. 1998, *ApJ*, 507, 759

Arnaboldi, M., Freeman, K. C., Hui, X., et al. 1994, *ESO Messenger*, 76, 40

Arnaboldi, M., Freeman, K. C., Méndez, R. H., et al. 1996, *ApJ*, 472, 145

Binney, J. J., Davies, R. L., & Illingworth, G. D. 1990, *ApJ*, 361, 78

Buote, D. A., & Canizares, C. R. 1994, *ApJ*, 427, 86

Buote, D. A., & Canizares, C. R. 1997, *ApJ*, 474, 650

Ciardullo, R. 1995, *Highlights of Astronomy*, 10, 507

Ciardullo, R., Jacoby, G. H., & Dejonghe, H. B. 1993, *ApJ*, 414, 454

Ciardullo, R., Jacoby, G. H., Ford, H. C. & Neill, J. D. 1989, *ApJ*, 339, 53

da Costa, L. N., Willmer, C. N. A., Pellegrini, P. S. et al. 1998, *AJ*, 116, 1

Dejonghe, H., De Bruyne, V., Vauterin, P., & Zeilinger, W. W. 1996, *A&A*, 306, 363

de Vaucouleurs, G. & A., Corwin, H. G. et al. 1991, *Third Reference Catalogue of Bright Galaxies* (New York: Springer)

Douglas, N. G., Gerssen, J., Kuijken, K., & Merrifield, M. R. 2000, *MNRAS*, 316, 795

Douglas, N. G., & Taylor, K. 1999, *MNRAS*, 307, 190

Ferrarese, L., Mould, J. R., Kennicutt, R. C., et al. 2000, *ApJ*, 529, 745

Garcia, A. M. 1993, *A&AS*, 100, 47

Gerhard, O., Kronawitter, A., Saglia, R., & Bender, R. 2000, *AJ*, in press (astro-ph/0012381, 18 Dec 2000)

Hernquist, L. 1990, *ApJ*, 356, 359

Hui, X., Ford, H. C., Ciardullo, R., & Jacoby, G. H. 1993, *ApJ*, 414, 463

Hui, X., Ford, H. C., Freeman, K. C., & Dopita, M. A. 1995, *ApJ*, 449, 592

Jacoby, G. H. 1989, *ApJ*, 339, 39

Jacoby, G. H. 1997, in IAU Symp. 180, Planetary Nebulae, ed. H. J. Habing & H. J. G. L. M. Lamers (Dordrecht:Kluwer), p. 448

Jacoby, G. H., Ciardullo, R., & Ford, H.C. 1990, *ApJ*, 356, 332

Jacoby, G. H., Ciardullo, R., Ford, H.C., & Booth, J. 1989, *ApJ*, 344, 704

Jacoby, G. H., Quigley, R. J., & Africano, J. L. 1987, *PASP*, 99, 672

Loewenstein, M. & White, R. E. 1999, *ApJ*, 518, 50

Maraston, C. 1998, *MNRAS*, 300, 872

Méndez, R. H. 1999, in Post-Hipparcos Cosmic Candles, ed. A. Heck & F. Caputo, *Astrophys. and Space Science Library*, Vol. 237 (Dordrecht:Kluwer), p. 161

Méndez, R. H. & Soffner, T. 1997, *A&A*, 321, 898

Merritt, D. & Saha, P. 1993, *ApJ*, 409, 75

Oke, J. B. 1990, *AJ*, 99, 1621

Peletier, R. F., Davies, R. L., Illingworth, G. D. et al. 1990, *AJ*, 100, 1091

Saglia, R. P., Kronawitter, A., Gerhard, O., & Bender, R. 2000, *AJ*, 119, 153

Sansom, A. E., Hibbard, J. E., & Schweizer, F. 2000, *AJ*, 120, 1946

Sarazin, C. L., Irwin, J. A., & Bregman, J. N. 2000, *ApJ*, 544, L101

Schlegel, D. J., Finkbeiner, D. P., & Davis, M. 1998, *ApJ*, 500, 525

Schneider, S. E., Terzian, Y., Purgathofer, A., & Perinotto, M. 1983, *ApJS*, 52, 399

Stetson, P. B. 1987, *PASP*, 99, 191

Taylor, K. 1977, *MNRAS*, 181, 475

Tonry, J. L., Dressler, A., Blakeslee, J. P. et al. 2000, astro-ph/0011223 (10 Nov 2000)

Trager, S. C., Faber, S. M., Worthey, G., & González, J. J. 2000, *AJ*, 120, 165

Tremblay, B., Merritt, D., & Williams, T. B. 1995, *ApJ*, 443, L5

Fig. 1.— On-band (left), off-band (center), and dispersed (grism + on-band) (right) subimages taken from the W field combined FORS1 exposures of NGC 4697 (see section 3). The area shown is  $130 \times 130$  pixels, and is located 750 pixels west from the center of NGC 4697. Two PN candidates are visible in the on-band, absent in the off-band, and remain as point sources in the dispersed image, but shifted some 330 pixels to the right along the direction of dispersion. This shift, once calibrated, gives the wavelength of the detected emission line.

Fig. 2.— The plus signs indicate the  $x, y$  coordinates, in pixels, of the 190 undispersed slit positions used for the wavelength calibration. For slits at  $x > 1650$  pixels, the comparison spectrum falls partly outside of the CCD and no reliable wavelength calibration is possible.

Fig. 3.— To save space we have added images 30T12:48 (undispersed) and 30T12:50 (dispersed), which correspond to calibration position 4 (see Table 1). Here we show a small portion of this added image. The separation between slits is very small, and when the slits are vertically aligned they look like a continuous line. At the extreme left we see the undispersed images of 4 of the 19 vertically aligned slits; the dispersed images to the right correspond to Cd and He comparison lines at 4678, 4713, 4799, 4921, 5015 and 5085 Å. These 6 lines were used for wavelength calibration at all the grid positions shown in Fig. 2. The weak comparison line at 5047 Å was not used.

Fig. 4.— On this image of NGC 7293, taken from the Digitized Sky Survey, we have indicated with a white line the approximate position of our 19 FORS slits. The telescope was pointed so that this part of the nebula fell on 6 different  $x$  coordinates across the CCD (see Fig. 5). The radial velocity of NGC 7293 on the white line is  $-20 \pm 10$  km s $^{-1}$ .

Fig. 5.— The plus signs indicate the  $x, y$  coordinates, in pixels, of the 114 (19×6) undispersed slit positions used in NGC 7293. In this case no effort was made to produce a perfect vertical alignment. The descending diagonal is a reference line used to calculate the small distortion corrections (see Section 6).

Fig. 6.— NGC 4697, on-band combined image, Field E. Two of the blades used in FORS to define slits for multi-object spectroscopy were used as “fingers” to cover very bright stars in the field. The size of this field is  $6.8 \times 6.8$  arc minutes. The x-axis of the CCD is oriented in the direction of the major axis of the galaxy, at a position angle of 66 degrees (from N through E). Therefore, using compass names, in this figure NNW is up, and ENE is to the left.

Fig. 7.— NGC 4697, on-band combined image, Field W. Two “fingers” were used here as well. Size and orientation of the field as in Fig. 6.

Fig. 8.— NGC 4697, on-band – off-band difference image, part of Field E. Some parts of the image near saturation level were replaced by zeros; the ellipse marks the center of the galaxy. The PNs appear as black dots.

Fig. 9.— NGC 4697, on-band – off-band difference image, part of Field W. Same description as in Fig. 8.

Fig. 10.— NGC 4697, unmedianed – medianed grism image, Field E (same part of galaxy as in Fig. 8).

Fig. 11.— NGC 4697, unmedianed – medianed grism image, Field W (same part of galaxy as in Fig. 9).

Fig. 12.— The mags  $m(5007)$  of 211 PNs were measured in both fields, E and W. Here we compare both measurements. From the dispersion we estimate RMS errors of 0.1 and 0.2 mag for  $m(5007)$  brighter and fainter than 26.5, respectively.

Fig. 13.— The number of PNs brighter than  $m(5007)=27.6$  detected within squares of  $220 \times 220$  pixels, plotted as a function of the background counts per pixel in each square. The relation is linear below 1000 counts per pixel, but not above that limit.

Fig. 14.— The squares represent the observed [O III]  $\lambda 5007$  PNLF of NGC 4697, with the 328 data binned into 0.2 mag intervals. The apparent magnitudes  $m(5007)$  have been transformed into absolute magnitudes  $M(5007)$  by adopting an extinction correction of 0.105 mag and a distance modulus  $m - M = 30.1$ . The three lines are PNLF simulations (Méndez and Soffner 1997) for three different sample sizes: 2500, 3500 and 4900 PNs. From the sample size it is possible to estimate the PN formation rate (see text). The adoption of a distance modulus 29.9 or 30.3 instead of 30.1 would ruin the fit.

Fig. 15.— The observed PNLF is now compared with the analytical representation (exponential + fixed or universal cutoff) proposed by Ciardullo et al. (1989). The adopted distance modulus is again 30.1. An attempt to fit the “overluminous” PN would result in a slightly smaller distance estimate. In fact the brightest PN is not “overluminous”; its existence is predicted by the simulations shown in Fig. 14. For sample sizes of the order of several thousands, as we have here, the “universal cutoff” representation of the PNLF begins to show some limitations, leading to slightly too small distances, as discussed by Méndez (1999).

Fig. 16.— The “slitless” heliocentric radial velocities of NGC 7293 measured at the 114 undispersed positions shown in Fig. 5. The velocities, in  $\text{km s}^{-1}$ , are plotted as a function of the distance from the undispersed position to the diagonal reference line shown in Fig. 5.

These distances, defined positive above the reference line and negative below, are expressed in hundreds of pixels. The solid line is a cubic parabola fitting the distribution.

Fig. 17.— The velocities of NGC 7293 plotted in Fig. 16 have been corrected as described in the text. From this figure we estimate that the calibration errors in slitless velocities are below  $20 \text{ km s}^{-1}$ .

Fig. 18.— The velocities of 165 PNs measured in both the E and W fields are compared. The velocities are expressed in thousands of  $\text{km s}^{-1}$ . The standard deviation is  $36 \text{ km s}^{-1}$ .

Fig. 19.— Positions of the 535 PNs in arc seconds relative to the center of light of NGC 4697.

Fig. 20.— Velocities of 531 PNs as a function of their  $x$  coordinates in arc seconds relative to the center of light of NGC 4697.

Fig. 21.— Velocities of 531 PNs as a function of their  $y$  coordinates in arc seconds relative to the center of light of NGC 4697.

Fig. 22.— The 531 PN velocities have been separated in 8 groups according to their  $x$  coordinates, and in the central groups (which include many PNs) we have selected only PNs near the major axis. The  $y$  coordinate limits for the 6 central groups, from left to right, are the following (in arc seconds):  $\pm 40, \pm 40, \pm 20, \pm 20, \pm 40, \pm 40$ . The squares with error bars indicate the average velocity within each group, plotted at the position of the average  $x$  coordinate of the group. The numbers of PNs per group, from left to right, are the following: 26, 23, 34, 33, 39, 25, 23 and 16. The plus signs represent velocities measured on integrated light spectra along the major axis by Binney et al. (1990). The effective radius  $R_e$  is 95 arc seconds.

Fig. 23.— Here we consider only velocities of PNs within  $\pm 10$  arc seconds of the major axis. The selected PN velocities have been separated in 6 groups according to their  $x$  coordinates. The squares with error bars indicate the average velocity within each group, plotted at the position of the average  $x$  coordinate of the group. The numbers of PNs per group, from left to right, are the following: 11, 14, 15, 16, 12, and 9. The plus signs have the same meaning as in Fig. 22.

Fig. 24.— The plus signs are line-of-sight velocity dispersions measured by Binney et al. (1990) on integrated light spectra along the major axis. The squares with error bars are our line-of-sight velocity dispersions from the PN velocities. The PNs have been separated in 8 groups according to angular distance from the center, as explained in the text. The numbers of PNs per group are: center NE, 108; center SW, 83; inner ring NE, 81; inner ring SW, 92;

second ring NE, 57; second ring SW, 39; outer zone NE, 26; outer zone SW, 16. The solid line is the analytical model by Hernquist (1990), with a constant M/L ratio and a total mass of  $1.9 \times 10^{11}$  solar masses, adopting  $R_e = 95$  arc seconds. A smaller  $R_e$  of 75 arc seconds would give a 10% smaller total mass.

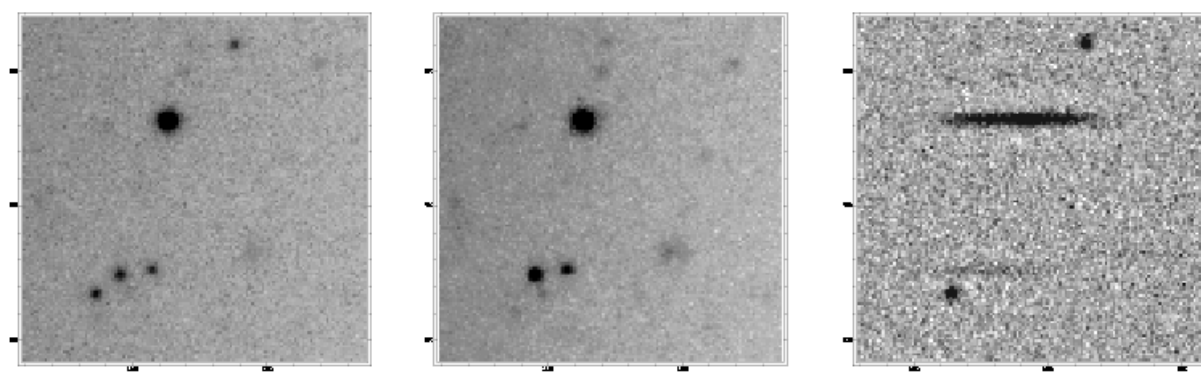


Fig. 1.— Figure 1

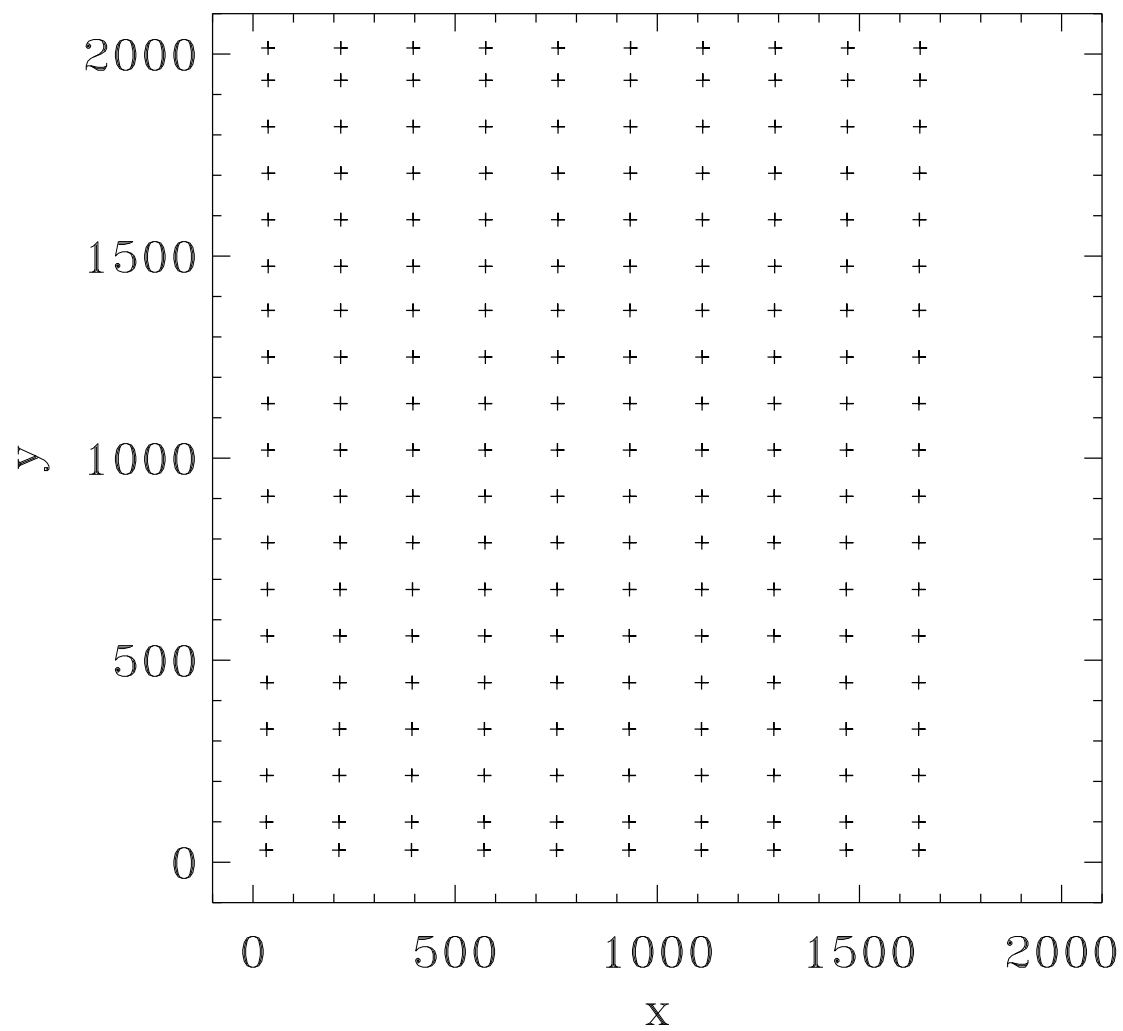


Fig. 2.— Figure 2

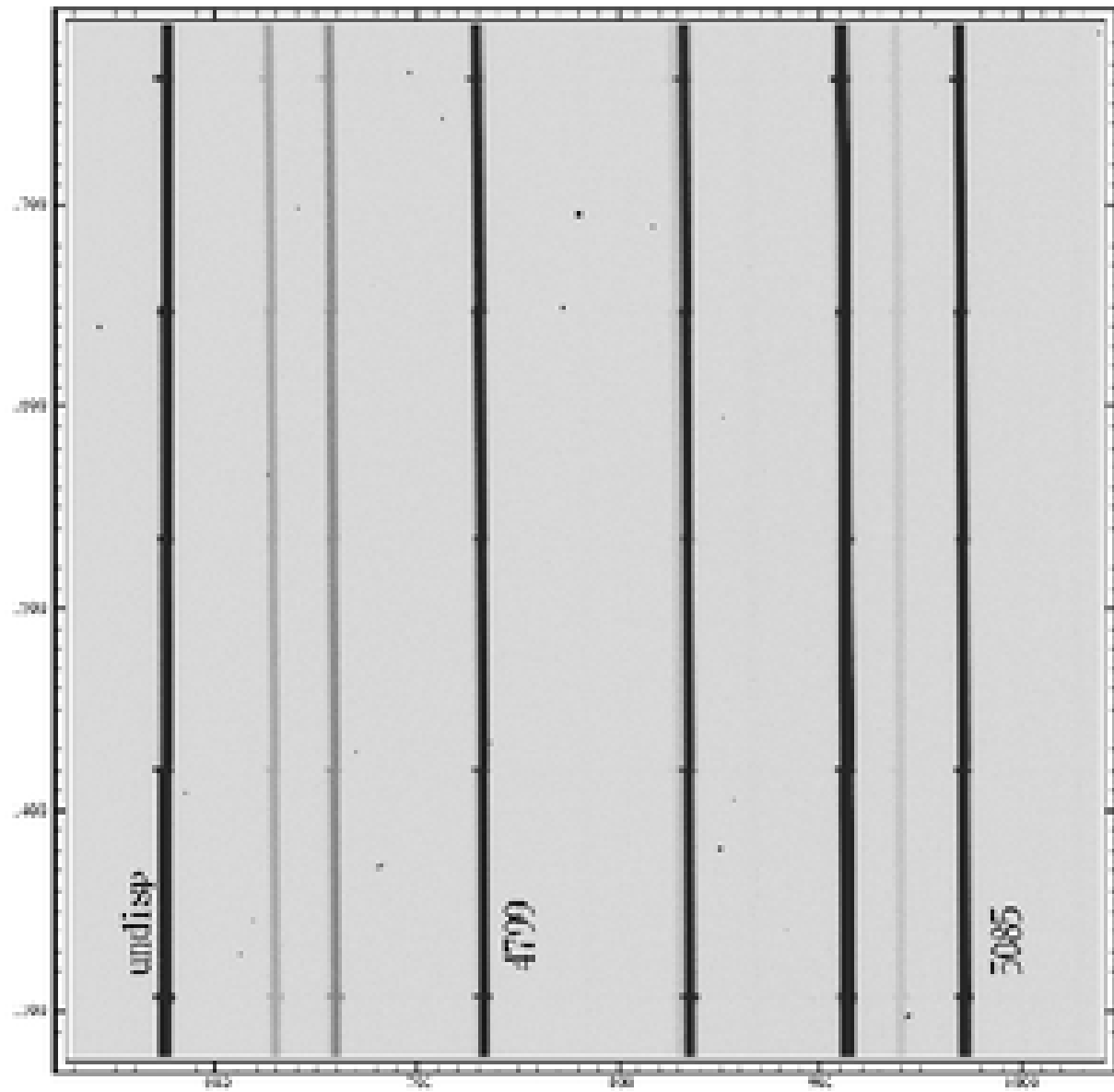


Fig. 3.— Figure 3

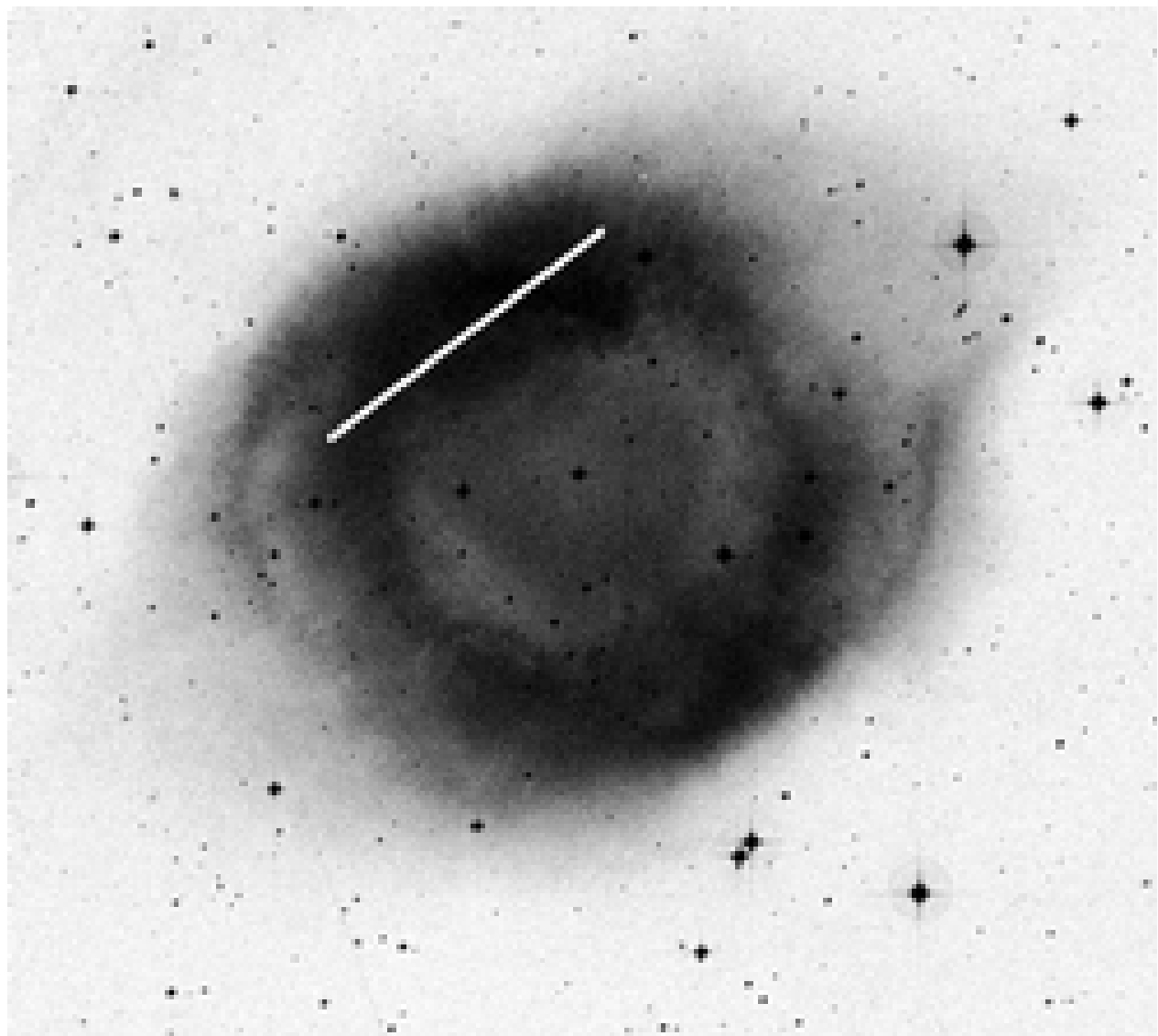


Fig. 4.— Figure 4

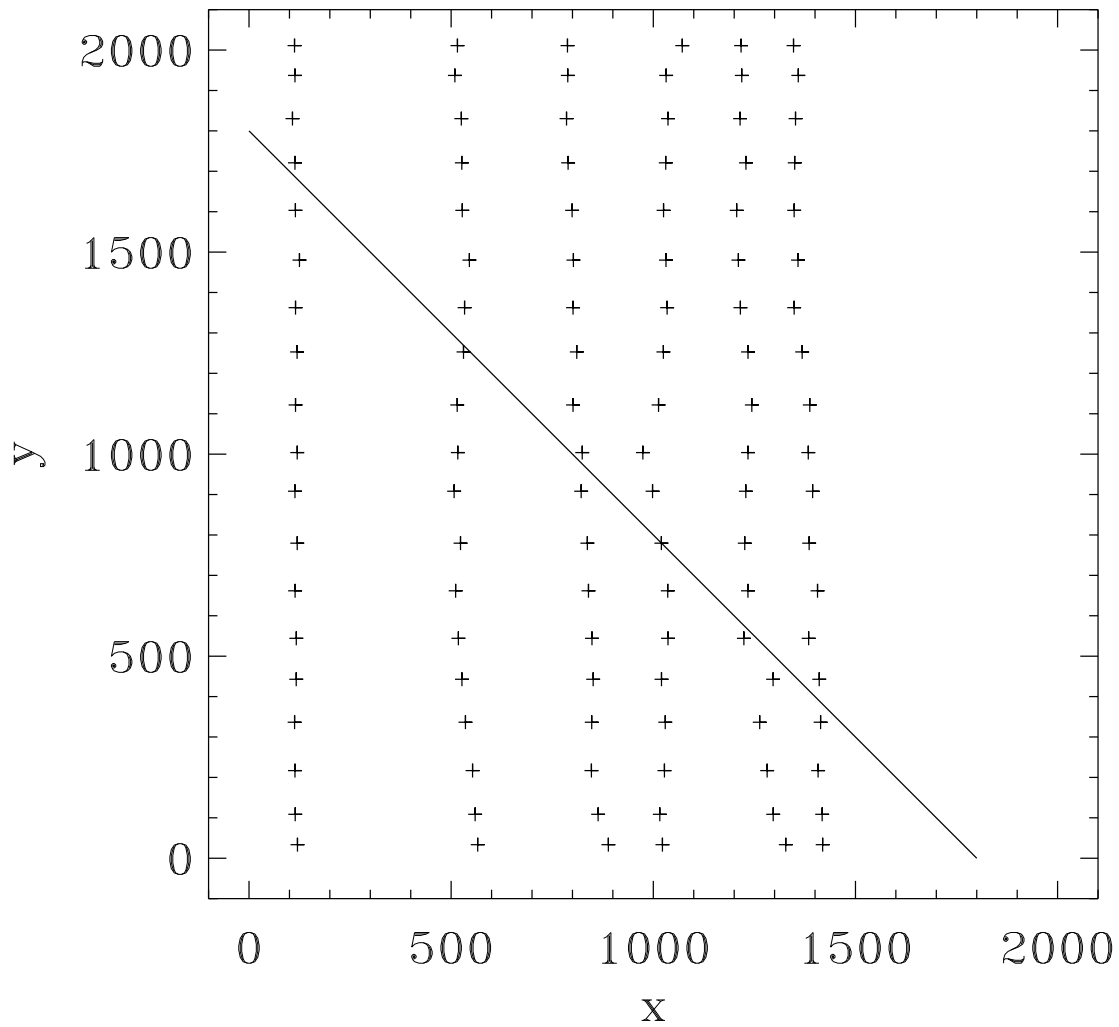


Fig. 5.— Figure 5

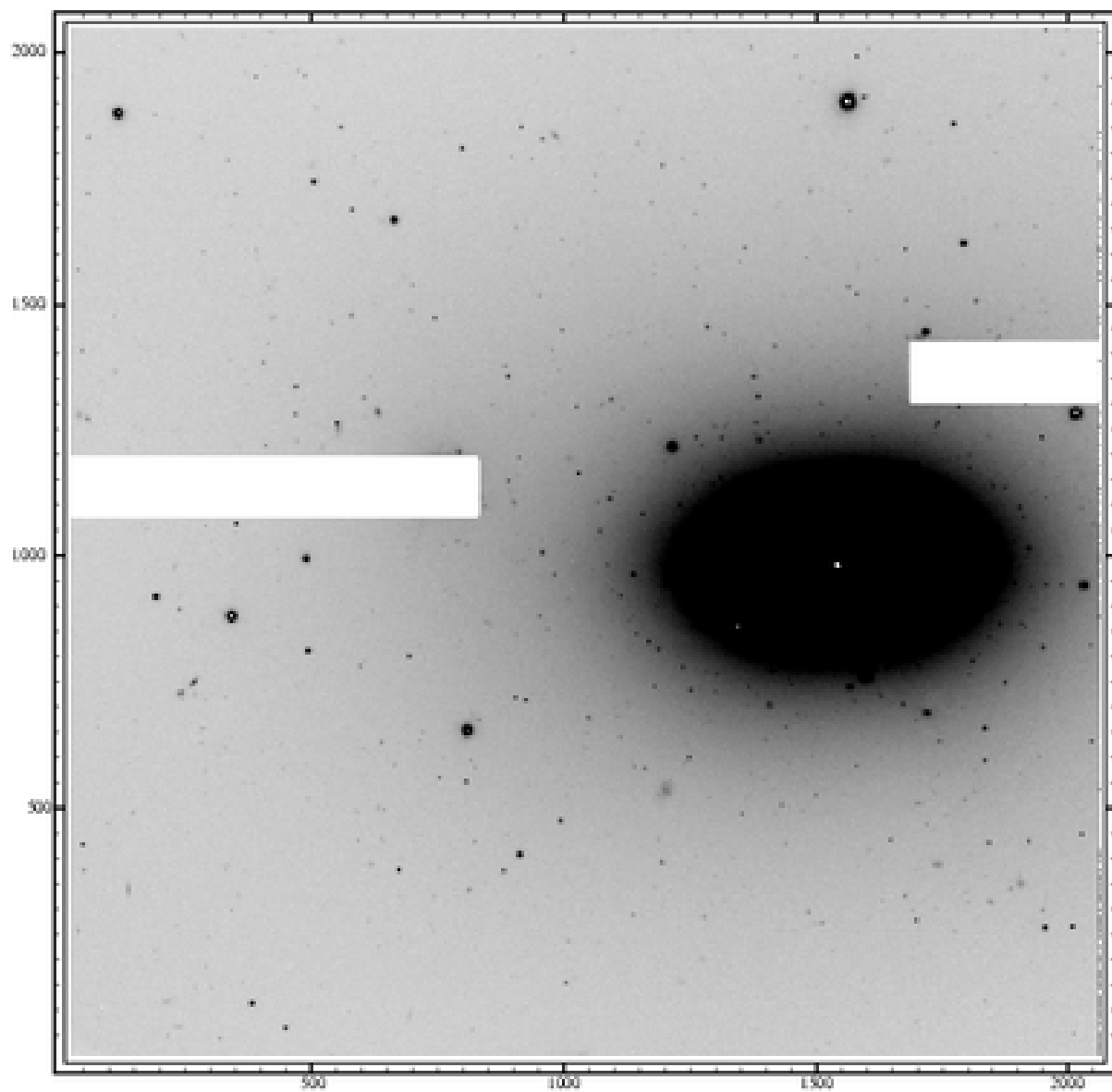


Fig. 6.— Figure 6

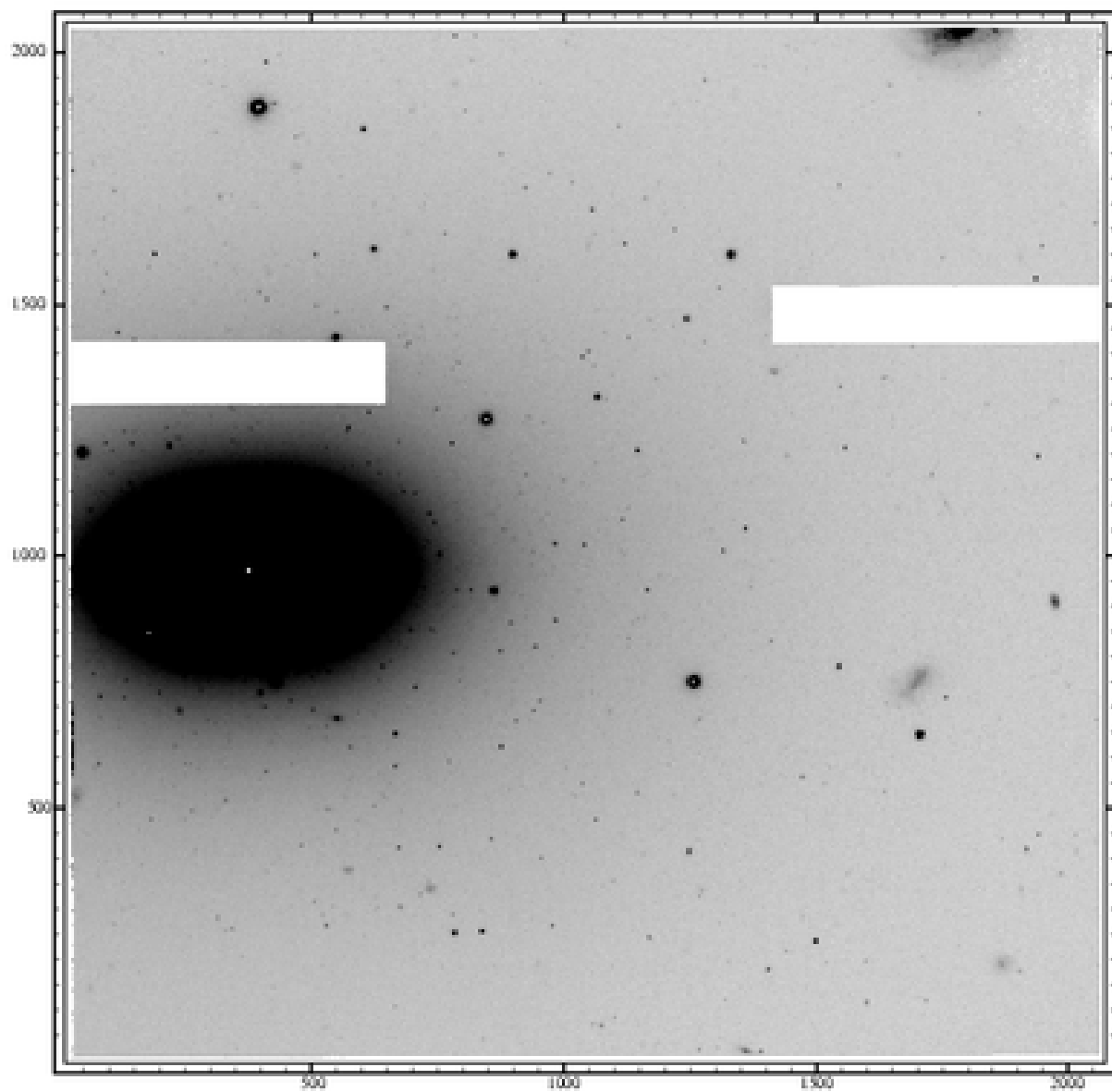


Fig. 7.— Figure 7

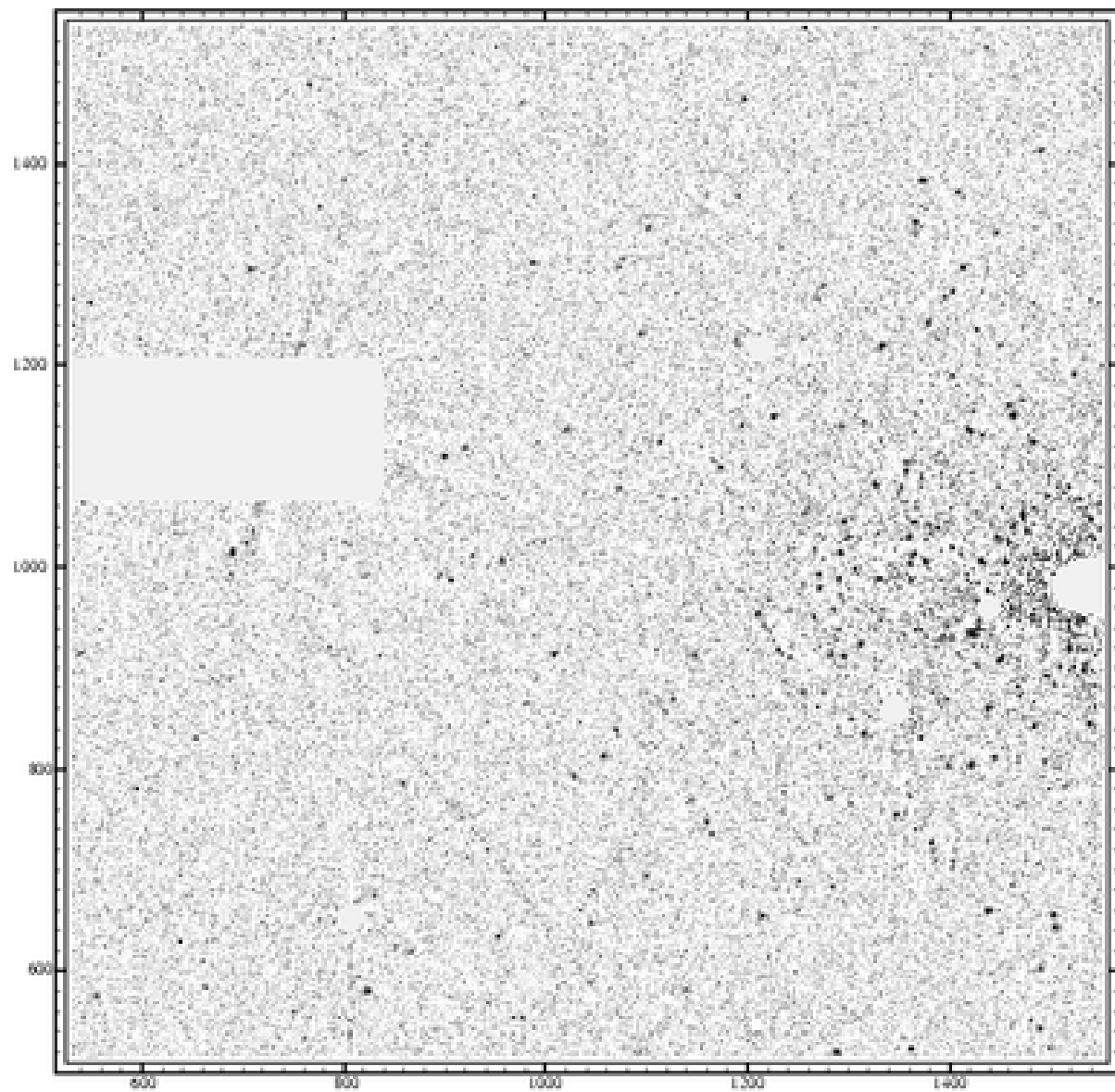


Fig. 8.— Figure 8

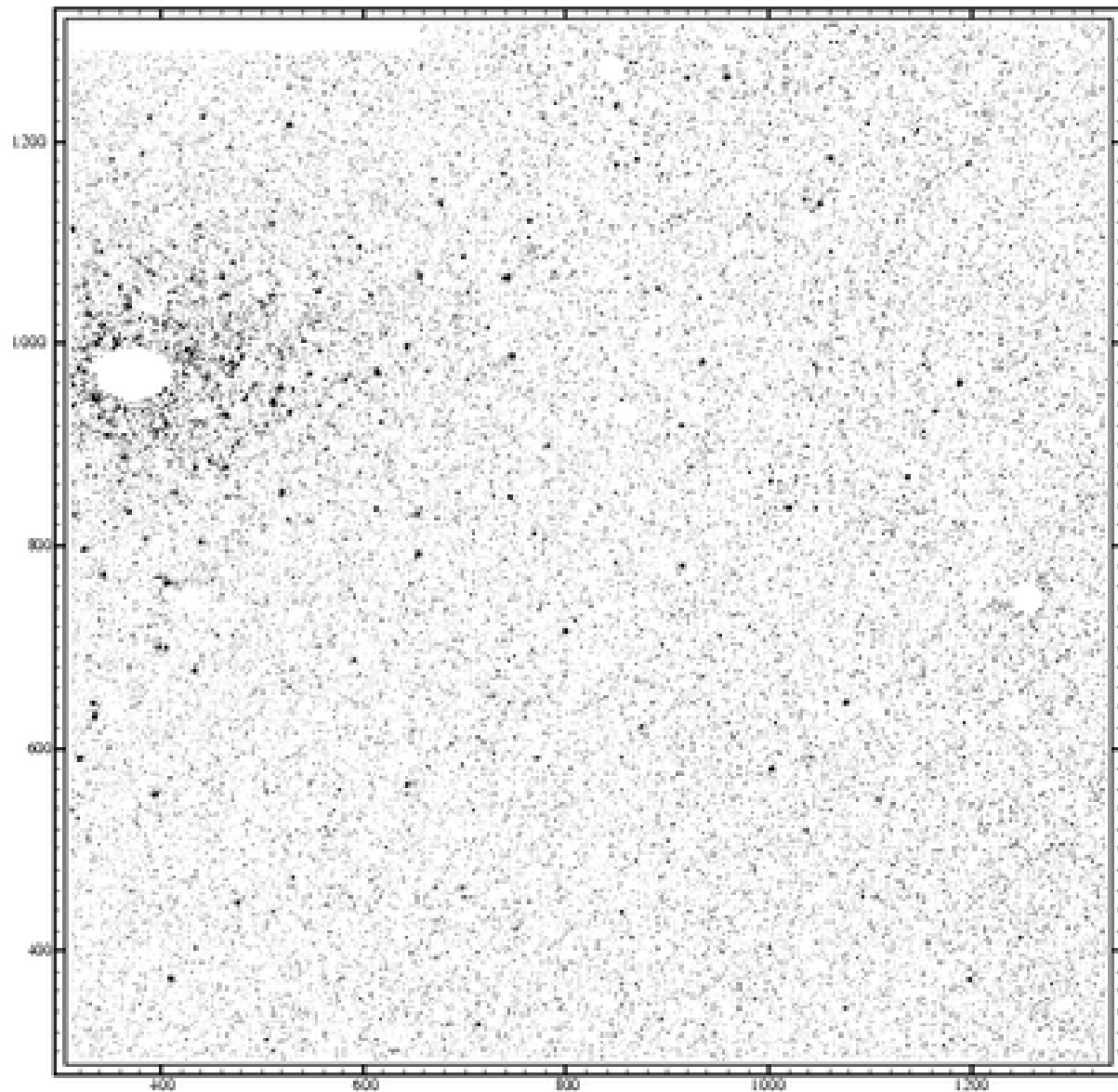


Fig. 9.— Figure 9

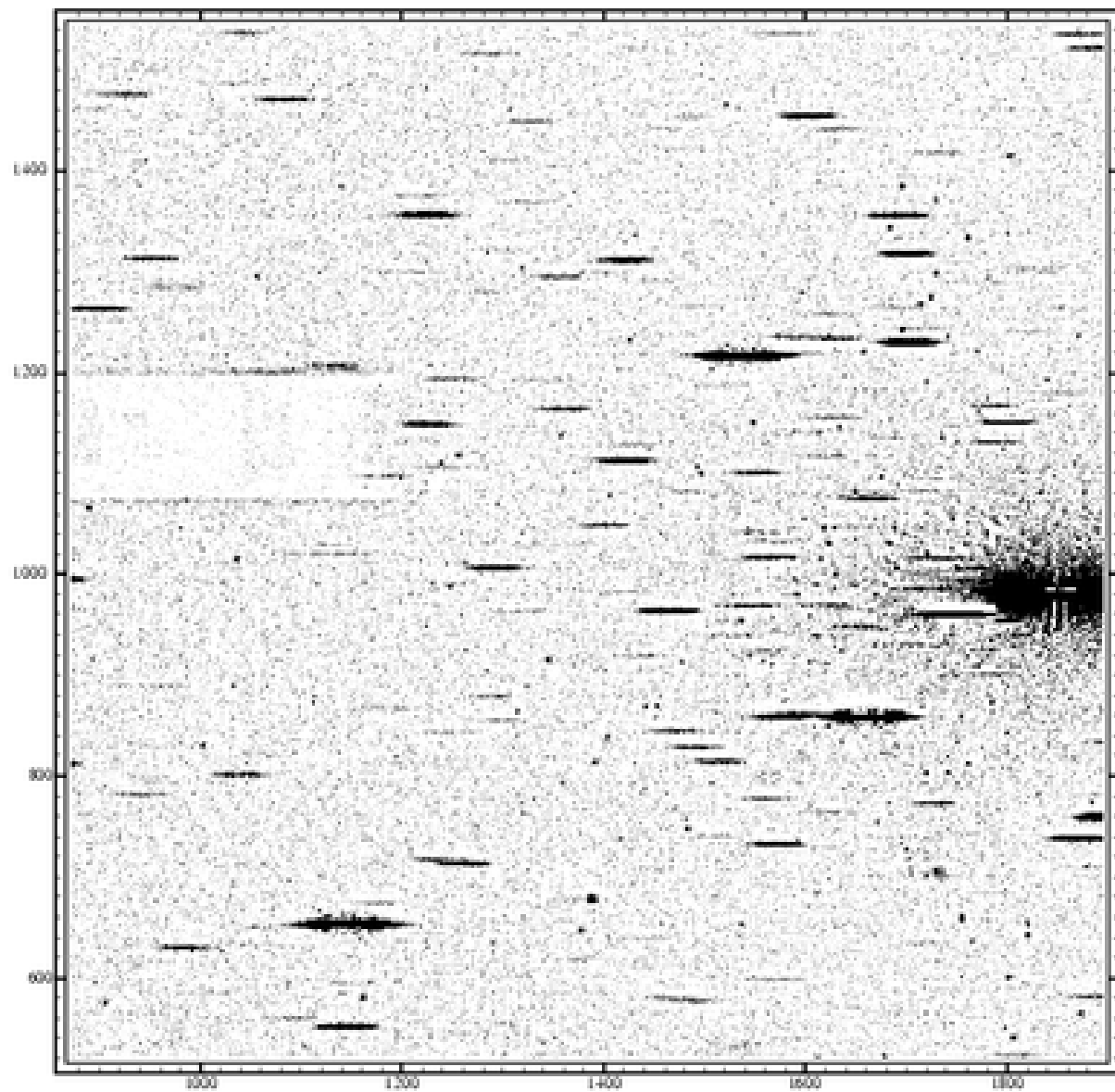


Fig. 10.— Figure 10

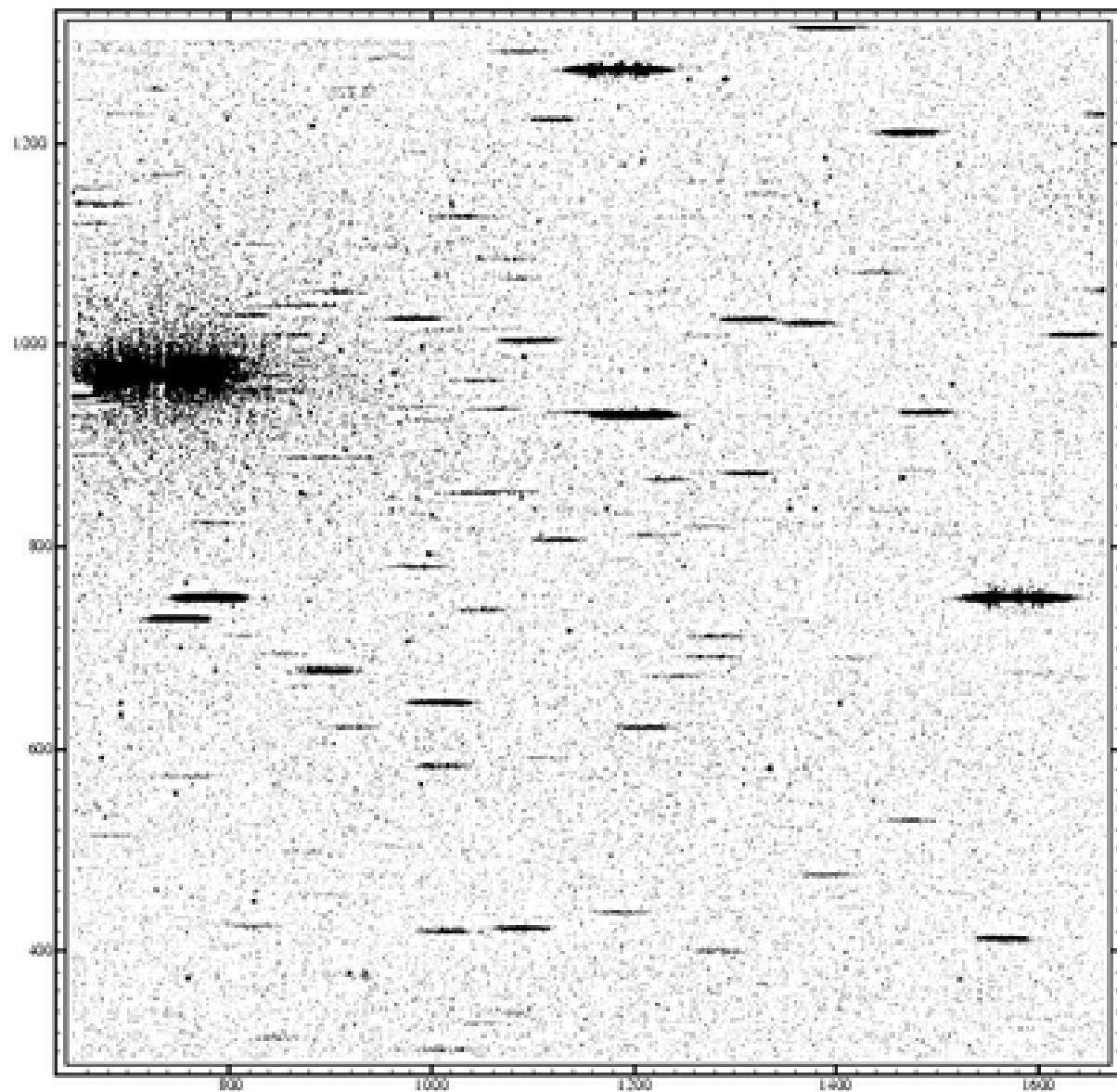


Fig. 11.— Figure 11

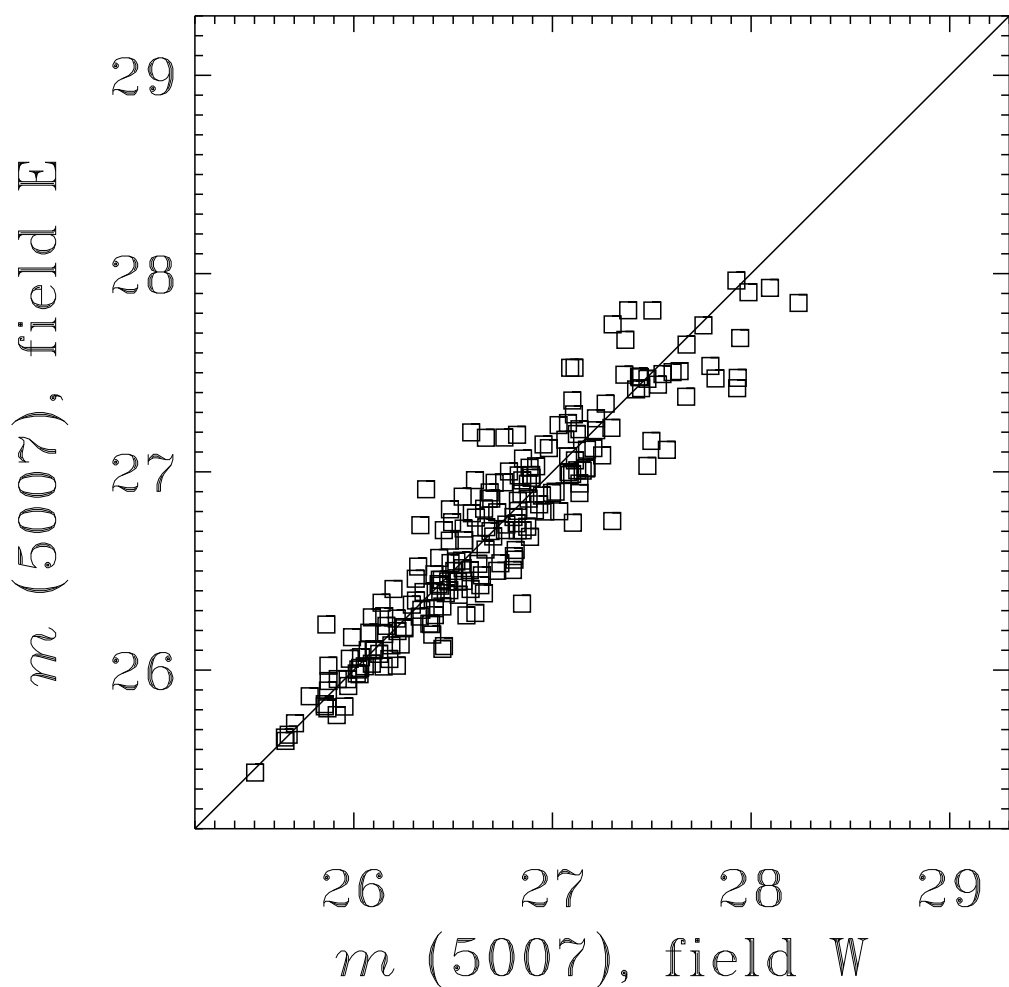


Fig. 12.— Figure 12

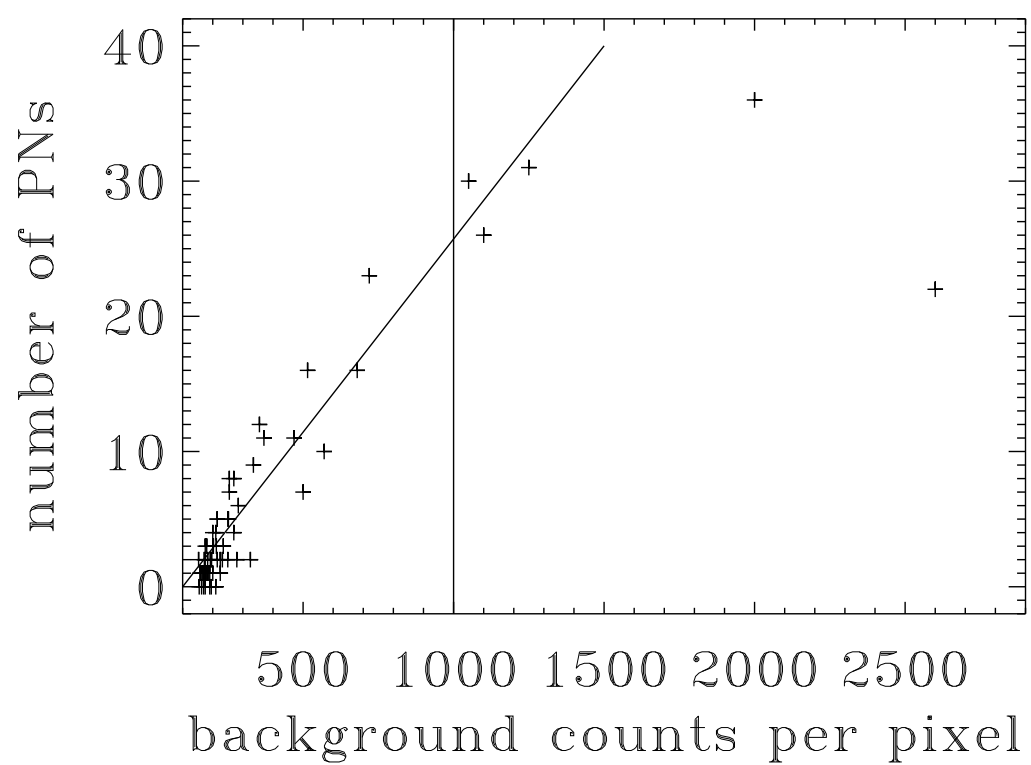


Fig. 13.— Figure 13

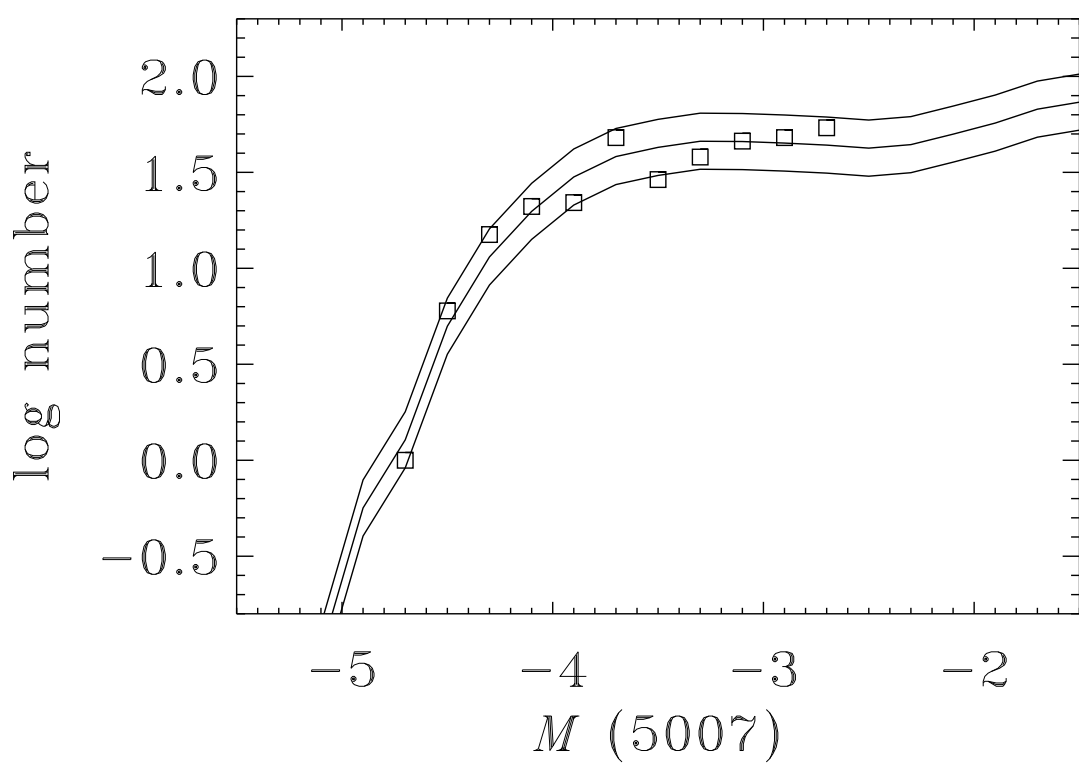


Fig. 14.— Figure 14

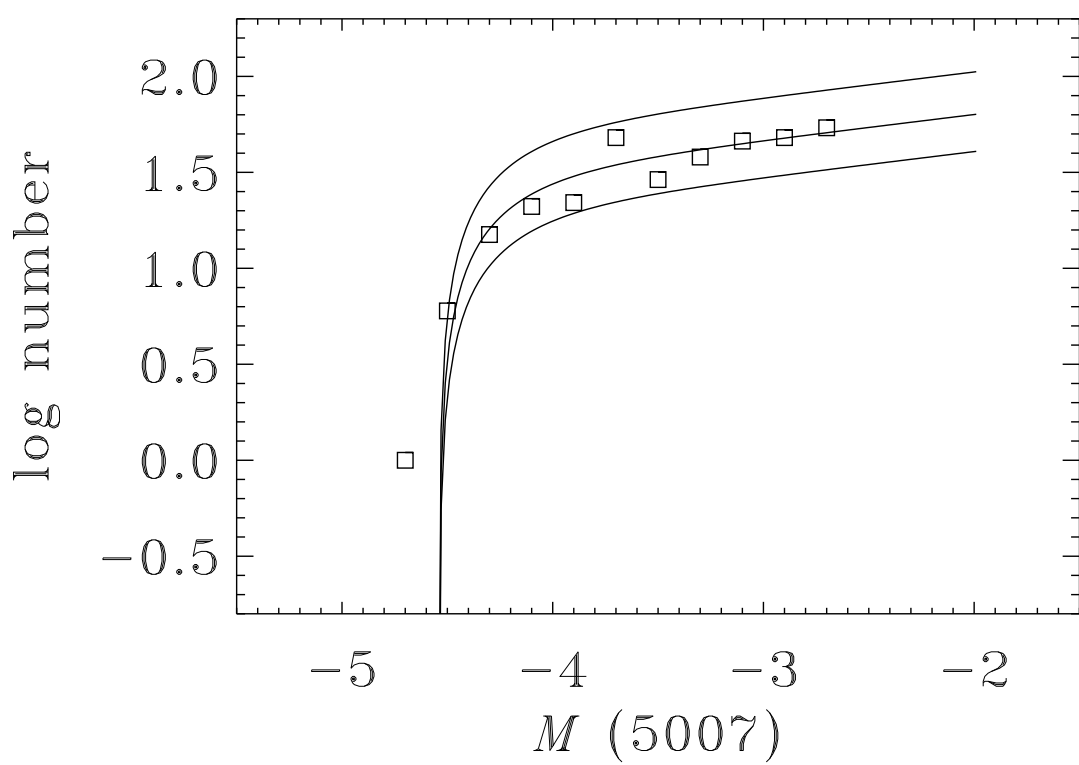


Fig. 15.— Figure 15

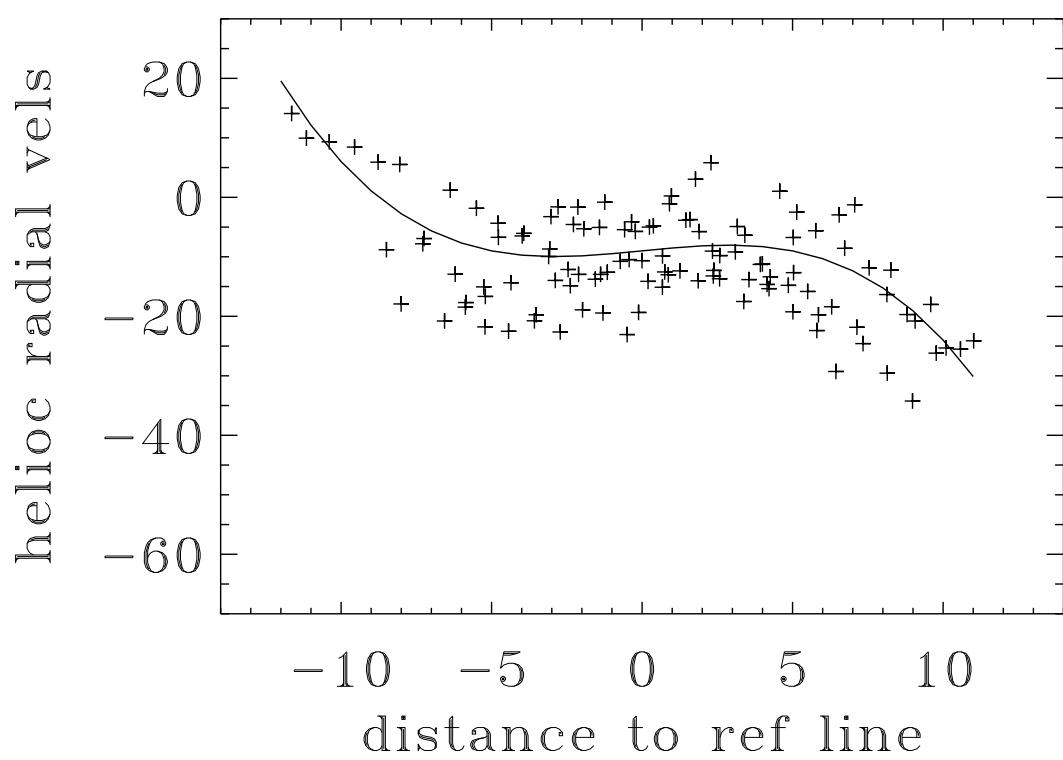


Fig. 16.— Figure 16

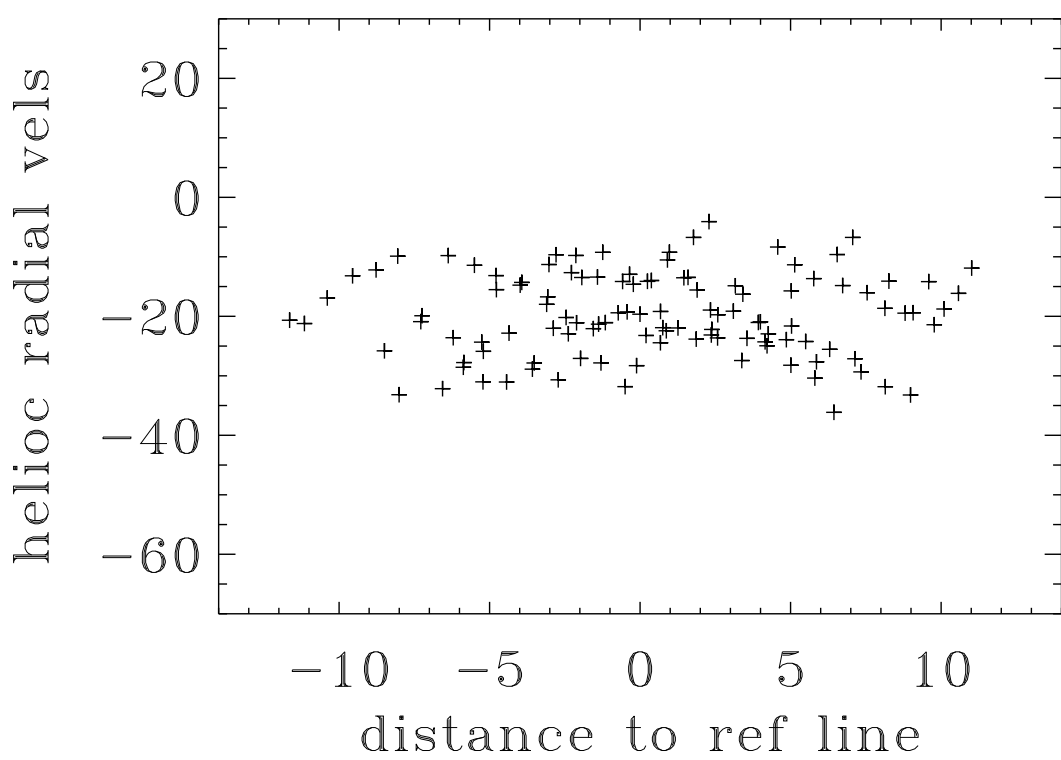


Fig. 17.— Figure 17

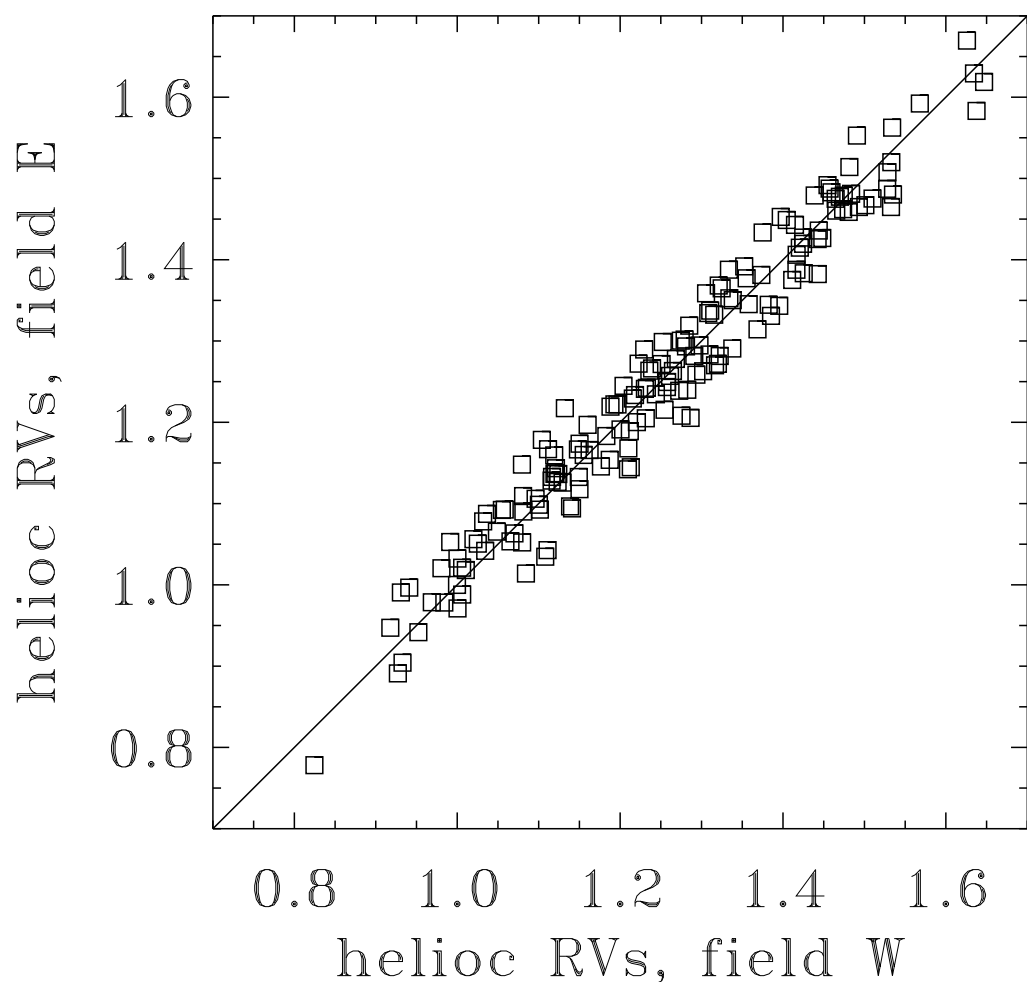


Fig. 18.— Figure 18

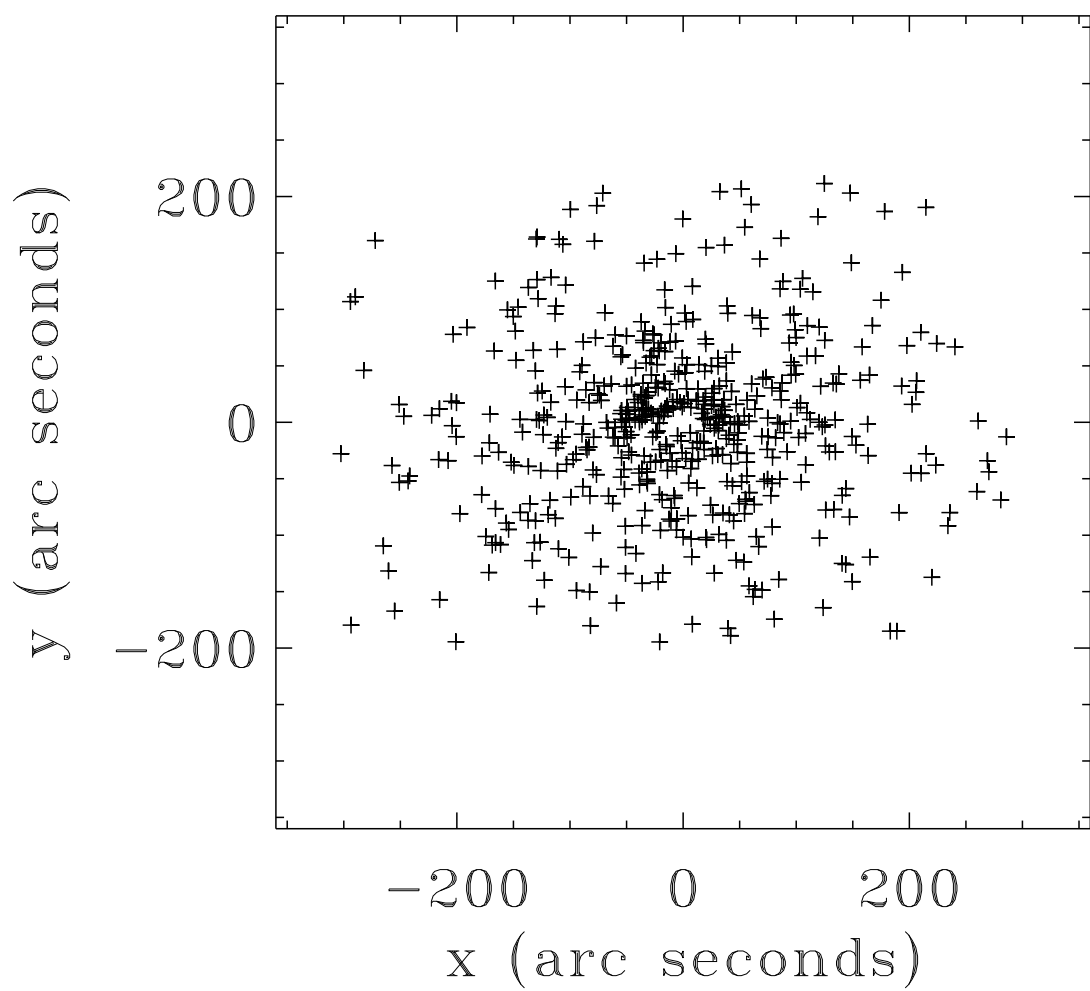


Fig. 19.— Figure 19

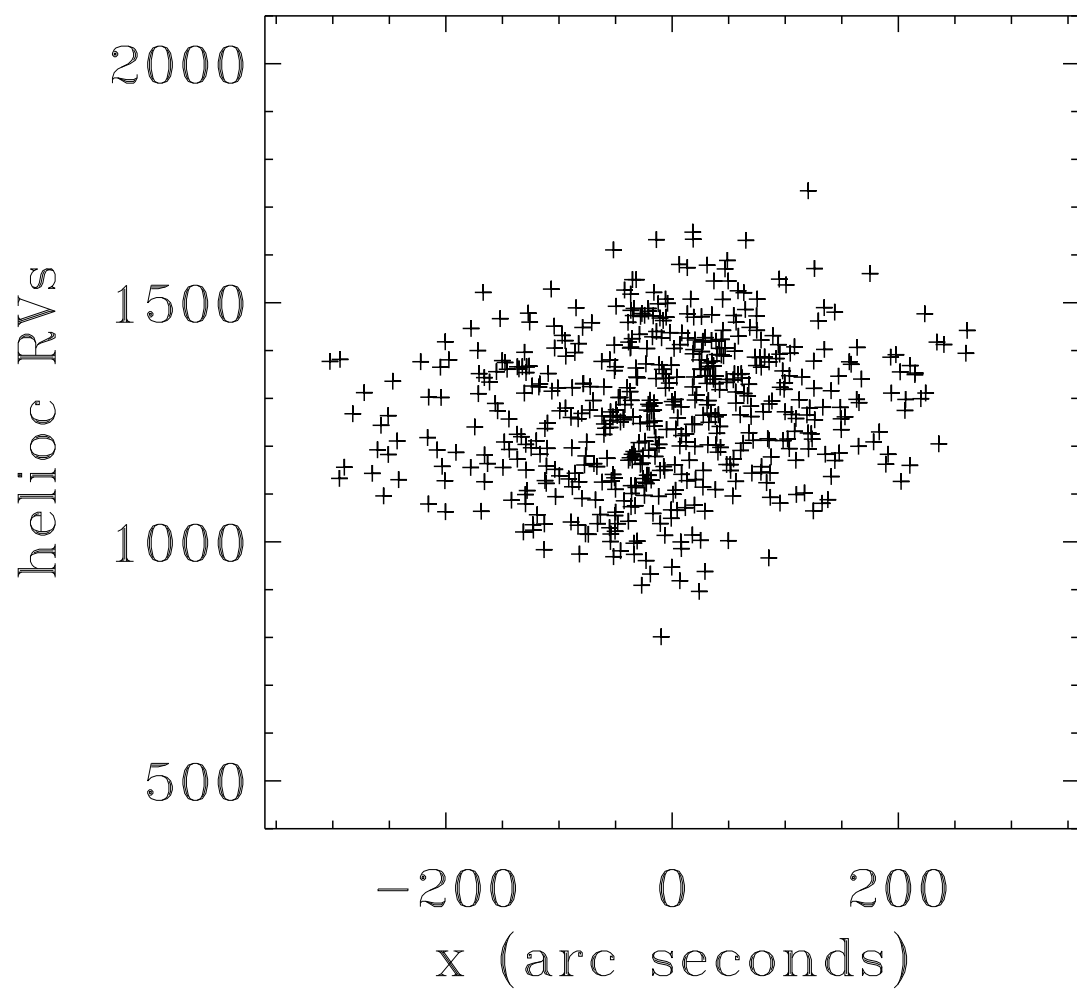


Fig. 20.— Figure 20

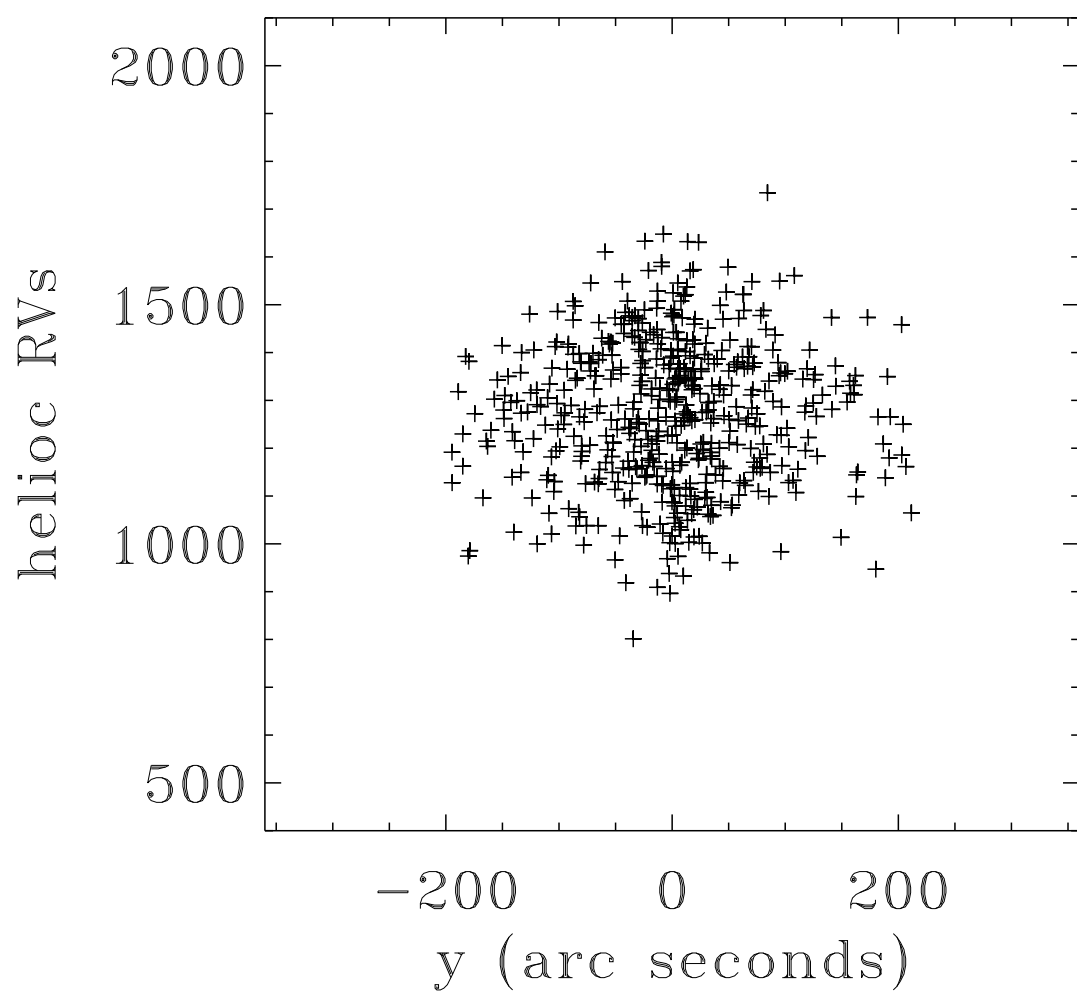


Fig. 21.— Figure 21

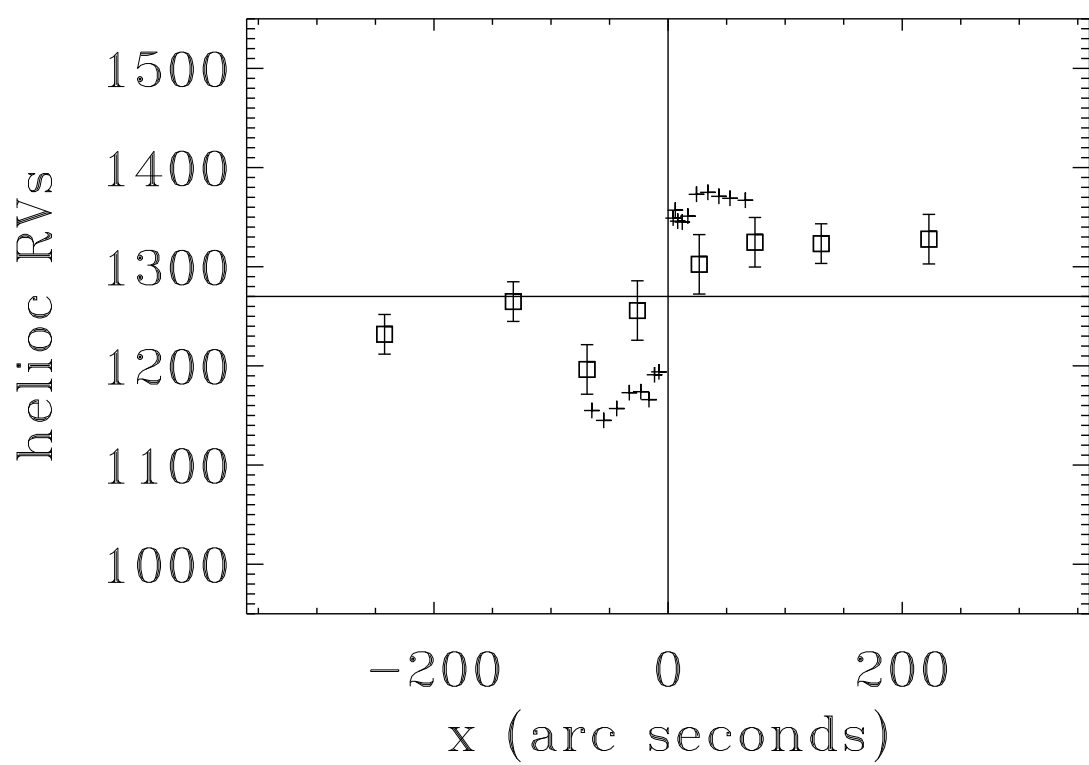


Fig. 22.— Figure 22

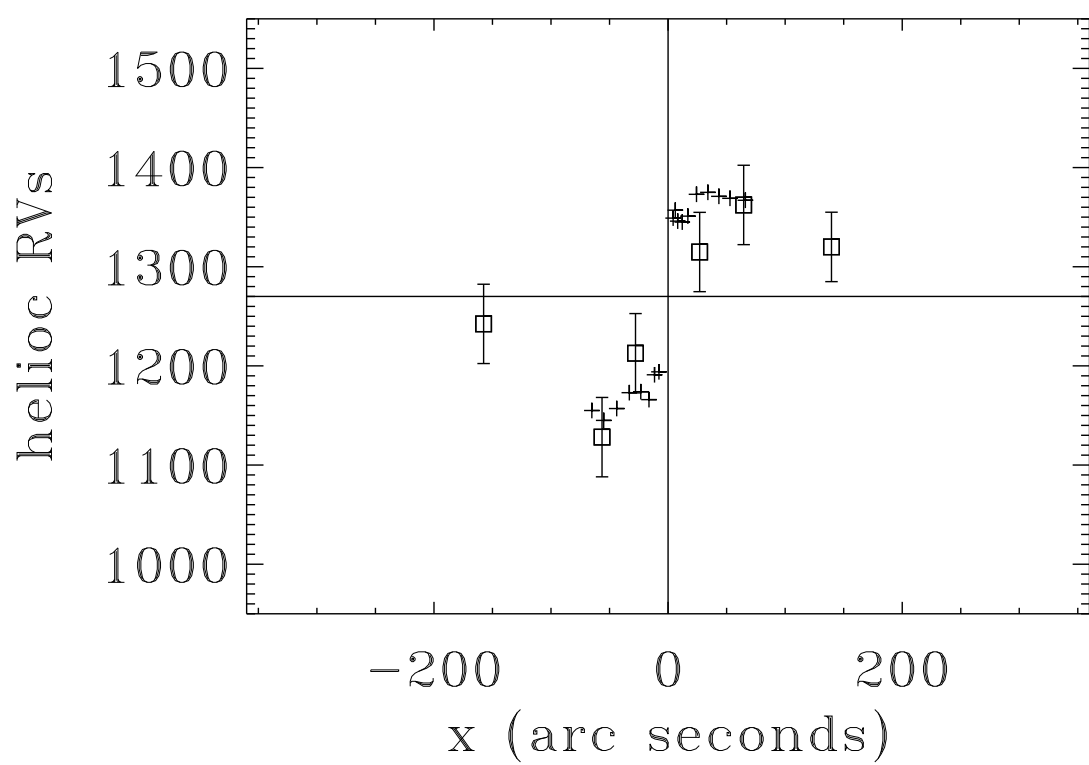


Fig. 23.— Figure 23

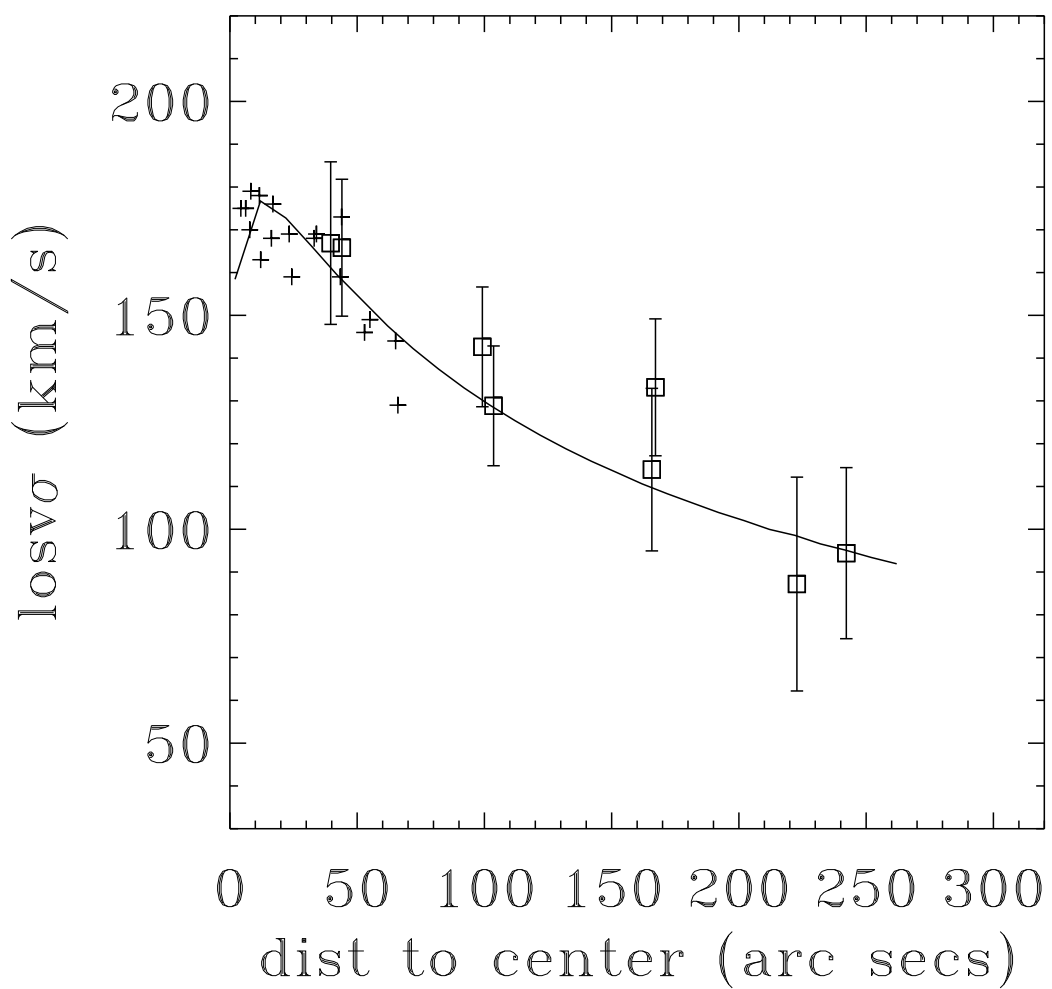


Fig. 24.— Figure 24

Table 1. Observations and calibrations

Field	Config	FORS1 CCD frame identification	exp (s)	Air mass <sup>a</sup>
He 2-118	on-band	FORS.1999-04-20T08:36:34.818.fits	20	1.26
He 2-118	grism+on	FORS.1999-04-20T08:37:56.133.fits	20	1.26
NGC 4697 W	off-band	FORS.1999-04-22T01:40:24.000.fits	600	1.17
NGC 4697 W	on-band	FORS.1999-04-22T01:51:23.924.fits	1200	1.14
NGC 4697 W	grism+on	FORS.1999-04-22T02:12:35.052.fits	2400	1.10
NGC 4697 W	off-band	FORS.1999-04-22T03:01:23.624.fits	900	1.06
NGC 4697 W	on-band	FORS.1999-04-22T03:17:23.062.fits	1200	1.06
NGC 4697 W	grism+on	FORS.1999-04-22T03:38:32.814.fits	2400	1.07
NGC 4697 W	grism+on	FORS.1999-04-22T04:24:25.502.fits	2400	1.11
NGC 4697 W	off-band	FORS.1999-04-22T05:14:19.274.fits	900	1.19
NGC 4697 W	on-band	FORS.1999-04-22T05:30:18.150.fits	1200	1.24
He 2-118	on-band	FORS.1999-04-22T08:25:39.484.fits	10	1.27
He 2-118	grism+on	FORS.1999-04-22T08:26:56.090.fits	20	1.27
NGC 4697 E	off-band	FORS.2000-05-29T23:09:36.121.fits	900	1.16
NGC 4697 E	on-band	FORS.2000-05-29T23:25:48.288.fits	1500	1.12
NGC 4697 E	grism+on	FORS.2000-05-29T23:52:02.001.fits	2400	1.08
NGC 4697 E	off-band	FORS.2000-05-30T00:35:04.237.fits	900	1.06
NGC 4697 E	on-band	FORS.2000-05-30T00:51:11.048.fits	1500	1.06
NGC 4697 E	grism+on	FORS.2000-05-30T01:17:23.306.fits	2400	1.08
NGC 4697 E	off-band	FORS.2000-05-30T01:59:12.334.fits	900	1.10
NGC 4697 E	on-band	FORS.2000-05-30T02:15:15.528.fits	1500	1.14
NGC 4697 E	grism+on	FORS.2000-05-30T02:41:28.870.fits	2400	1.23
G 138-31	on-band	FORS.2000-05-30T04:07:08.131.fits	100	1.21
NGC 7293 p1	on-band	FORS.2000-05-30T09:33:18.900.fits	100	1.04
NGC 7293 p1	grism+on	FORS.2000-05-30T09:36:30.313.fits	250	1.03
NGC 7293 p2	on-band	FORS.2000-05-30T10:23:51.849.fits	100	1.00
NGC 7293 p2	grism+on	FORS.2000-05-30T10:27:02.299.fits	250	1.00
MOS cal. p1	undisp.	FORS.2000-05-30T11:37:59.703.fits	10	—
MOS cal. p1	disp.	FORS.2000-05-30T11:40:03.923.fits	300	—
MOS cal. p2	undisp.	FORS.2000-05-30T11:54:53.993.fits	10	—
MOS cal. p2	disp.	FORS.2000-05-30T11:56:58.370.fits	300	—

Table 1—Continued

Field	Config	FORS1 CCD frame identification	exp (s)	Air mass <sup>a</sup>
MOS cal. p3	undisp.	FORS.2000-05-30T12:29:15.781.fits	10	—
MOS cal. p3	disp.	FORS.2000-05-30T12:31:20.217.fits	300	—
MOS cal. p4	undisp.	FORS.2000-05-30T12:48:53.658.fits	10	—
MOS cal. p4	disp.	FORS.2000-05-30T12:50:58.267.fits	300	—
MOS cal. p5	undisp.	FORS.2000-05-30T13:07:27.466.fits	10	—
MOS cal. p5	disp.	FORS.2000-05-30T13:09:32.060.fits	300	—
MOS cal. p6	undisp.	FORS.2000-05-30T13:33:04.556.fits	10	—
MOS cal. p6	disp.	FORS.2000-05-30T13:35:09.123.fits	300	—
MOS cal. p7	undisp.	FORS.2000-05-30T13:57:20.765.fits	10	—
MOS cal. p7	disp.	FORS.2000-05-30T13:59:25.251.fits	300	—
MOS cal. p8	undisp.	FORS.2000-05-30T14:17:05.835.fits	10	—
MOS cal. p8	disp.	FORS.2000-05-30T14:19:10.277.fits	300	—
MOS cal. p9	undisp.	FORS.2000-05-30T14:49:00.448.fits	10	—
MOS cal. p9	disp.	FORS.2000-05-30T14:51:05.629.fits	300	—
MOS cal. p10	undisp.	FORS.2000-05-30T15:13:21.145.fits	10	—
MOS cal. p10	disp.	FORS.2000-05-30T15:15:25.757.fits	300	—
NGC 4697 W	off-band	FORS.2000-05-30T23:01:16.768.fits	900	1.17
NGC 4697 W	off-band	FORS.2000-05-30T23:17:22.665.fits	900	1.14
NGC 4697 W	on-band	FORS.2000-05-30T23:33:19.758.fits	1500	1.11
NGC 4697 W	grism+on	FORS.2000-05-31T00:00:04.556.fits	2400	1.07
NGC 4697 W	on-band	FORS.2000-05-31T00:42:06.004.fits	1800	1.06
NGC 4697 E	off-band	FORS.2000-05-31T01:56:56.533.fits	900	1.10
NGC 4697 E	on-band	FORS.2000-05-31T02:12:50.309.fits	1500	1.14
NGC 4697 E	grism+on	FORS.2000-05-31T02:38:59.384.fits	2400	1.23
G 138-31	on-band	FORS.2000-05-31T03:24:08.942.fits	100	1.26
NGC 7293 p3	on-band	FORS.2000-05-31T08:34:14.790.fits	100	1.13
NGC 7293 p3	grism+on	FORS.2000-05-31T08:37:05.265.fits	250	1.12
NGC 7293 p4	on-band	FORS.2000-05-31T08:54:43.811.fits	100	1.09
NGC 7293 p4	grism+on	FORS.2000-05-31T08:57:33.414.fits	250	1.08
NGC 7293 p5	on-band	FORS.2000-05-31T09:13:37.789.fits	100	1.06
NGC 7293 p5	grism+on	FORS.2000-05-31T09:16:28.264.fits	250	1.05

Table 1—Continued

Field	Config	FORS1 CCD frame identification	exp (s)	Air mass <sup>a</sup>
NGC 7293 p6	on-band	FORS.2000-05-31T09:58:28.841.fits	100	1.01
NGC 7293 p6	grism+on	FORS.2000-05-31T10:01:18.615.fits	250	1.01
NGC 4697 E	off-band	FORS.2000-05-31T23:15:10.254.fits	900	1.14
NGC 4697 E	on-band	FORS.2000-05-31T23:31:04.416.fits	1500	1.10
NGC 4697 E	grism+on	FORS.2000-05-31T23:57:14.651.fits	2400	1.07
NGC 4697 W	off-band	FORS.2000-06-01T00:43:25.603.fits	900	1.06
NGC 4697 W	on-band	FORS.2000-06-01T00:59:19.970.fits	1500	1.06
NGC 4697 W	grism+on	FORS.2000-06-01T01:25:29.402.fits	2400	1.09

<sup>a</sup>the air masses correspond to the middle of each exposure